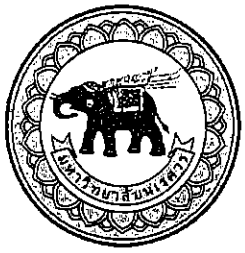

รายงานวิจัยฉบับสมบูรณ์

การค้นหา Cataclysmic Variables คาบการโคจรสั้น จากเซอเวย์การแปรค่าความสว่าง

อมรรัตน์ อังเวโรจน์วิทย์
ภาควิชาฟิสิกส์ คณะวิทยาศาสตร์ มหาวิทยาลัยนเรศวร

ธันวาคม 2561

บทคัดย่อ

รหัสโครงการ: R2561B087
ชื่อโครงการ: การค้นหา Cataclysmic Variables คาบการโคจรสั้นจากเซอเวย์การแปรค่าความสว่าง
ชื่อนักวิจัย: ผศ.ดร. อมรรัตน์ อังเวโรจน์วิทย์
ภาควิชาฟิสิกส์ คณะวิทยาศาสตร์ มหาวิทยาลัยนเรศวร
E-mail Address: amornrata@nu.ac.th
ระยะเวลาโครงการ: 9 ตุลาคม 2560 ถึง 8 ตุลาคม 2561

เรานำเสนอข้อมูลอนุกรมเวลาทางโฟโตเมตรีของ cataclysmic variables (CVs) ที่ค้นพบใหม่จากสมบัติทางการระเบิดใหญ่ซึ่งตรวจพบใน Catalina Real-Time Transient Survey (CRTS), Sloan Digital Sky Survey (SDSS) และ All-Sky Automated Survey for Supernovae (ASASSN) จำนวน 16 ระบบ เราสามารถวัดคาบ superhump (P_{sh}) ของ CVs เหล่านี้ได้ทั้งหมดจำนวน 8 ระบบ โดยเราค้นพบ CVs คาบการโคจรสั้น (P_{sh} < 2 ชั่วโมง) จำนวน 8 ระบบ ได้แก่ ASASSN-16bi (Psh = 83.8 นาที), ASASSN-16cq (Psh = 85.4 นาที), ASASSN-16da (Psh = 82.5 นาที), ASASSN-16ez (Psh = 82.9 นาที), ASASSN-16fu (Psh = 81.96 นาที), ASASSN-16gh (Psh = 92.06 นาที), ASASSN-16lf (Psh = 89.76 นาที) และ ASASSN-16bh มีคาบ superhump ประมาณ ค่าคาบการโคจรที่น้อยที่สุด (period minimum) ของ CVs (Psh = 78.99 นาที) โดยเราจำแนก CVs เหล่านี้ว่าเป็น SU UMa dwarf novae นอกจากนี้เรายังค้นพบ AM CVn จำนวน 2 ระบบ โดยมีคาบ superhump ดังนี้ CSS150211:091017-200813 (Psh = 29.67 นาที) และ ASASSN-15sz (Psh = 37.53 นาที)

คำหลัก: Cataclysmic variables, dwarf novae, SU UMa, AM CVn

สารบัญ

บทที่		หน้า
	บทคัดย่อ	ข
	Abstract	ค
	สารบัญ	ง
	สารบัญรูป	จ
	สารบัญตาราง	ฉ
1	**บทนำ**	1
2	**การสังเกตการณ์และการรีดิวซ์ข้อมูล**	3
	2.1 การสังเกตการณ์	3
	2.2 การรีดิวซ์ข้อมูล	7
3	**การวิเคราะห์ข้อมูล**	8
	3.1 การสร้างกราฟแสง	8
	3.2 การวิเคราะห์กราฟแสง	18
4	**สรุป**	28
Output		28
ภาคผนวก		29

สารบัญรูป

รูปที่		หน้า
1	กราฟแสงของ CSS150211:091017-200813	10
2	กราฟแสงของ ASASSN-15sz	10
3	กราฟแสงของ ASASSN-16bf	11
4	กราฟแสงของ ASASSN-16bh	11
5	กราฟแสงของ ASASSN-16bi	12
6	กราฟแสงของ ASASSN-16by	12
7	กราฟแสงของ ASASSN-16cg	13
8	กราฟแสงของ ASASSN-16cq	13
9	กราฟแสงของ ASASSN-16da	14
10	กราฟแสงของ ASASSN-16er	14
11	กราฟแสงของ ASASSN-16ez	15
12	กราฟแสงของ ASASSN-16fi	15
13	กราฟแสงของ ASASSN-16fu	16
14	กราฟแสงของ ASASSN-16gh	16
15	กราฟแสงของ ASASSN-16lt	17
16	กราฟแสงของ SDSSJ124043.43+671035.9	17
17	Scargle periodogram และ phase folded ของ CSS150211:091017-200813	19
18	Scargle periodogram และ phase folded ของ ASASSN-15sz	19
19	Scargle periodogram ของ ASASSN-16bf	20
20	Scargle periodogram และ phase folded ของ ASASSN-16bh	20
21	Scargle periodogram และ phase folded ของ ASASSN-16bi	21
22	Scargle periodogram ของ ASASSN-16by	21
23	Scargle periodogram ของ ASASSN-16cg	22
24	Scargle periodogram และ phase folded ของ ASASSN-16cq	22
25	Scargle periodogram และ phase folded ของ ASASSN-16da	23
26	Scargle periodogram ของ ASASSN-16er	23
27	Scargle periodogram และ phase folded ของ ASASSN-16ez	24
28	Scargle periodogram ของ ASASSN-16fi	24
29	Scargle periodogram และ phase folded ของ ASASSN-16fu	25
30	Scargle periodogram และ phase folded ของ ASASSN-16gh	25
31	Scargle periodogram และ phase folded ของ ASASSN-16lf	26
32	Scargle periodogram ของ SDSSJ124043.43+671035.9	26

สารบัญตาราง

ตารางที่		หน้า
1	รายละเอียดของการสังเกตการณ์	4
2	รายละเอียดของกราฟแสง	9

บทที่ 1
บทนำ

Cataclysmic Variables (CVs) เป็นระบบดาวคู่แบบใกล้ชิดชนิดกึ่งแตะกันที่ประกอบด้วยดาวแคระขาว (white dwarf) และดาวมวลต่ำในแถบลำดับหลัก (low-mass main sequence) ที่มีมวลเต็มผิวห่อหุ้มของโรชช์ (Roche lobe) และกำลังถ่ายเทมวลสารสู่ดาวแคระขาว วิวัฒนาการของ CVs ถูกขับเคลื่อนด้วยการสูญเสียโมเมนตัมเชิงมุมผ่านการกระบวนการ magnetic braking (Verbunt & Zwaan 1981; Rappaport และคณะ 1983) และ gravitational radiation (Faulkner 1971; Paczynski & Sienkiewicz 1981) ซึ่งจะทำให้ CVs มีวิวัฒนาการไปในทางคาบการโคจรที่สั้นลง จนกระทั่งดาวในแถบลำดับหลักมีมวลต่ำเกิน ซึ่งจะทำให้กระบวนการเผาผลาญไฮโดรเจนที่บริเวณแกนกลางหยุดลงและดาวอยู่ในสถานะดีเจนเนอเรต ส่งผลให้รัศมีเพิ่มขึ้นในขณะที่มวลมีค่าลดลง จากผลดังกล่าว CVs จะมีวิวัฒนาการถึงคาบการโคจรที่น้อยที่สุด (minimum orbital period) และจะวิวัฒนาการย้อนกลับไปยังคาบการโคจรที่ยาวขึ้น แบบจำลองมาตรฐานทำนายคาบการโคจรที่น้อยที่ประมาณ 65 นาที (Kolb & Baraffe 1999; Howell และคณะ 2001) ในขณะที่การสังเกตพบว่ามีค่าประมาณ 75-80 นาที (เช่น Ritter & Kolb 2003; Knigge 2006; Gänsicke และคณะ 2009) นอกจากนี้แบบจำลองมาตรฐานยังแสดงให้เห็นว่าประมาณ 99% จำนวนประชากรของ CVs ควรมีคาบการโคจรสั้น (P_{orb} < 2 h) และประมาณ 70% ของ CVs คาบการโคจรสั้นเหล่านี้ควรมีวิวัฒนาการผ่านคาบการโคจรที่น้อยที่สุดไปแล้ว (Kolb 1993; Howell และคณะ 1997) เนื่องจากวิวัฒนาการของคาบการโคจรจะช้าลงที่บริเวณคาบการโคจรที่สั้นที่สุด ดังนั้นเราควรพบ CVs จำนวนมากที่บริเวณคาบการโคจรที่น้อยที่สุด แต่แผนภาพการกระจายตัวของประชากรของ CVs ที่ได้จากการสังเกตกลับไม่พบการสะสมของระบบที่บริเวณคาบการโคจรที่น้อยที่สุดตามที่ทฤษฎีทำนาย (Kolb & Baraffe 1999; Willems และคณะ 2005)

ความขัดแย้งระหว่างสิ่งที่แบบจำลองทำนายและแผนภาพการกระจายตัวของประชากรของ CVs จากการสังเกต อาจเป็นผลมาจากความไม่แน่นอนของแบบจำลอง หรืออาจมาจากผลของการเลือกสังเกต (เช่น Gänsicke 2005) ในด้านการสังเกต กลุ่มตัวอย่างของ CVs ในหลายเซอร์เวย์ ที่ผ่านการคัดเลือกด้วยวิธีเดียวกันได้ถูกก่อตั้งขึ้นด้วยวัตถุประสงค์หลักคือ เพื่อลดผลของการเลือกสังเกตที่พบในกลุ่มตัวอย่างของ CVs ที่ถูกค้นพบก่อนหน้านี้ ตัวอย่างเซอร์เวย์เหล่านี้ เช่น Palomar Green Survey (Ringwald 1993) Hamburg Quasar Survey (Gänsicke และคณะ 2002; Aungwerojwit และคณะ 2006) Sloan Digital Sky Survey (Szkody และคณะ 2002, 2003, 2004, 2005, 2006, 2007, 2009, 2011)) โดยในปัจจุบัน SDSS เป็นเซอร์เวย์ที่สามารถค้นหา CVs ที่มีความสลัวได้มากที่สุด Gänsicke และคณะ (2009) แสดงให้เห็นว่าแผนภาพการกระจายตัวของ CVs จาก SDSS มีความแตกต่างอย่างสิ้นเชิงจากกลุ่มตัวอย่างของ CVs จากเซอร์เวย์อื่นๆ ในก่อนหน้านี้ทุกเซอร์เวย์ กล่าวคือ คณะผู้วิจัยพบ CVs จำนวนมากในช่วงคาบการโคจรที่ 80-86 นาที ทั้งนี้เนื่องมาจาก SDSS สามารถ 'มอง' วัตถุได้ลึกถึง i = 19 แมกนิจูด แต่อย่างไรก็ตามตำแหน่งของคาบการโคจรที่น้อยที่สุดของ CVs ใน SDSS ยังคงแตกต่างจากค่าที่แบบจำลองมาตรฐานทำนายมากกว่า 10 นาที และนอกจากนี้อัตราส่วนของ CVs คาบการโคจรสั้นต่อคาบการโคจรยาวที่ได้จากการสังเกตยังคงไม่เป็นไปตามที่แบบจำลองมาตรฐานทำนาย (Aungwerojwit และคณะ 2006; Pretorius และคณะ 2007; Pretorius & Knigge 2008)

เพื่อที่จะแก้ปัญหาเหล่านี้ เราได้เริ่มทำการค้นหา CVs ที่มีความสลัวอย่างแท้จริงในเซอร์เวย์การแปรค่าความสว่าง เช่น Catalina Real-time Transient Survey (CRTS; Drake และคณะ 2009) CRTS ครอบคลุมท้องฟ้าที่กาแล็กติกละติจูด $|b| > 10^{\circ}$ และเดคคลิเนชั่น $\delta > -30^{\circ}$ ดังนั้นจึงซ้อนทับกับพื้นที่ท้องฟ้าในการสำรวจของ SDSS พอดี และ All-Sky Automated Survey (ASAS) ซึ่งครอบคลุมท้องฟ้านอกระนาบกาแล็กติก (Shappee และคณะ 2014) และเซอร์เวย์เหล่านี้จะทำการถ่ายภาพวัตถุท้องฟ้าเป็นบริเวณกว้างอย่างต่อเนื่องเป็นระยะเวลาหลายปี CVs ส่วนใหญ่ใน CRTS และ ASAS ถูกค้นพบจากการระเบิด หรือเมื่อระบบถูกทำให้สว่างขึ้นมากถึง 2-5 แมกนิจูด ซึ่งขณะไม่เกิดการระเบิดมีแมกนิจูด > 19 ซึ่งสลัวเกินกว่าขีดจำกัดของเซอร์เวย์ ดังนั้นจากการอาศัยสมบัติทางการระเบิดของ CVs CRTS และ ASAS จึงสามารถค้นพบระบบที่อยู่ในพื้นที่ท้องฟ้าเดียวกันกับ SDSS แต่มีความสลัวมากกว่าหลายแมกนิจูด (สลัวถึงประมาณ 22 แมกนิจูด) ดังนั้น CVs จาก CRTS และ ASAS จะเป็นกลุ่มตัวอย่างของ CVs ที่สลัวที่สุดในปัจจุบัน การศึกษาความสัมพันธ์ของแอมปลิจูดและความถี่ของการระเบิดของ CVs ใน CRTS โดย Wils และคณะ (2010) แสดงให้เห็นว่าระบบที่สลัวใน CRTS เหล่านี้ประกอบด้วย วัตถุที่อยู่ไกล และ dwarf novae ที่มีความสลัวอย่างแท้จริง

ในโครงการวิจัยนี้เราจะวัดคาบการโคจรของกลุ่มตัวอย่างของ CV ใน CRTS, ASASSN และ SDSS ที่มีความสลัวที่สุด ($i \sim 22$) เพื่อใช้เป็นตัวกำหนดลักษณะของ CVs ที่มีความสลัวอย่างแท้จริง ซึ่งเป็นประชากรโดยส่วนใหญ่ของ CVs ทั้งหมด โดยใช้กล้องโทรทรรศน์ของสถาบันวิจัยดาราศาสตร์แห่งชาติ (องค์การมหาชน) ขนาด 0.5 เมตร และ 2.4 เมตร ตั้งอยู่ที่หอดูดาวแห่งชาติฯ บริเวณยอดดอยอินทนนท์ กล้องโทรทรรศน์ขนาด 0.6 เมตร PROMPT8 ตั้งอยู่ที่ หอดูดาวเซอโร โทโลโล ประเทศชิลี และกล้องโทรทรรศน์ควบคุมโดยระบบอัตโนมัติ 0.7 เมตร Gao Mei Gu (0.7m-TRT-GMG) ของสถาบันวิจัยดาราศาสตร์ ที่ติดตั้ง ณ หอดูดาวเกาเหมยกู่ (Gao Mei Gu Observatory) ประเทศจีน

บทที่ 2
การสังเกตการณ์และการรีดิวซ์ข้อมูล

2.1 การสังเกตการณ์

เราได้ทำการคัดเลือกและเก็บข้อมูลทางโฟโตเมตรีของ CVs จาก CRTS, ASASSN และ SDSS ซึ่งมีการแปรค่าความสว่างโดยมีความสว่างประมาณ >17 แมกนิจูด รวมถึงระบบที่มีการระเบิดใหญ่ในช่วง ~14-19 แมกนิจูด ที่มีอยู่ในภาพถ่ายของ SDSS และทำการเก็บข้อมูลโดยใช้กล้องโทรทรรศน์ขนาด 2.4 เมตร ต่อพ่วงกับซีซีดีถ่ายภาพความเร็วสูง ULTRASPEC (TNT/Uspec) ของหอดูดาวแห่งชาติเฉลิมพระเกียรติฯ ดอยอินทนนท์ กล้องโทรทรรศน์ขนาด 0.5 เมตร (0.5m-TNO) ของหอดูดาวแห่งชาติเฉลิมพระเกียรติฯ ดอยอินทนนท์ กล้องโทรทรรศน์ควบคุมโดยระบบอัตโนมัติ 0.7 เมตร Gao Mei Gu (0.7m-TRT-GMG) ของสถาบันวิจัยดาราศาสตร์ ที่ติดตั้ง ณ หอดูดาวเกาเหมยกู่ (Gao Mei Gu Observatory) ประเทศจีน และกล้องโทรทรรศน์ควบคุมโดยระบบอัตโนมัติ 0.6 เมตร PROMPT8 (P8) ของสถาบันวิจัยดาราศาสตร์ ที่ติดตั้ง ณ หอดูดาวเซอโร โทโลโล (Cerro Tololo Obseratory) ประเทศชิลี โดยมีวัตถุประสงค์เพื่อวัดคาบการโคจร และคาบ superhumps ของระบบ

CVs จาก CRTS, ASASSN และ SDSS ได้แก่ CSS150211:091017-200813, ASASSN-15sz, ASASSN-16af, ASASSN-16bf, ASASSN-16bi, ASASSN-16bh, ASASSN-16by, ASASSN-16cg, ASASSN-16cq, ASASSN-16da, ASASSN-16er, ASASSN-16ez, ASASSN-16fi, ASASSN-16fu, ASASSN-16gh, ASASSN-16lf, SDSSJ124043.43+671035.9

รายละเอียดของการสังเกตการณ์แสดงในตารางที่ 1

ตารางที่ 1 รายละเอียดของการสังเกตการณ์

Objects	mag	Date	Telescope	Filter	Exp. (s)	No.
CSS150211:091017-200813	19.3	20150212	P8	V	30	208
		20150213	P8	V	45	286
		20150214	P8	V	35	355
		20150215	P8	V	35	140
		20150216	P8	V	100	300
		20150217	P8	V	100	120
		20150219-26	P8	V	100	500
		20180114	TNT/USPEC	KG5	30	13
		20180222	TNT/USPEC	KG5	30	3
		20180318	TNT/USPEC	KG5	1	6431
		20180319	TNT/USPEC	KG5	3	4533
		20180320	TNT/USPEC	KG5	3	5157
ASASSN-15sz	19.5	20151122	P8	V	10	520
		20151123	P8	V	10	432
		20151124	P8	C	100	20
		20151126	P8	C	100	100
		20151127	P8	V	10	200
ASASSN-16af	g=21.9	20160112	P8	V	30	144
		20160113	P8	C	30	114
		20160114	P8	C	30	250
		20160115	P8	C	30	250
		20160116	P8	C	30	250
ASASSN-16bf	B=22.0	20160206	P8	C	100	120
		20160207	P8	C	100	140
ASASSN-16bi	R=20.6	20160208	P8	V	20	400
		20160209	P8	V	20	400
		20160210	P8	V	20	300
		20160111	P8	V	20	220
		20160212	P8	V	30	98
		20160213	P8	V	30	199
ASASSN-16bh	B=20.3	20160211	0.5m-TNO	V	15	782
		20160212	0.5m-TNO	V	15	1388

Objects	mag	Date	Telescope	Filter	Exp. (s)	No.
		20160213	0.5m-TNO	V	15	906
		20160213	0.7m-TRT-GMG	C	15	500
		20160214	0.5m-TNO	V	15	898
		20160214	P8	V	15	300
		20160215	P8	V	15	350
		20160216	0.7m-TRT-GMG	C	15	500
		20160216	P8	V	15	300
ASASSN-16by	no match	20160221	P8	C	40	148
		20160222	P8	C	40	185
		20160223	P8	C	40	178
ASASSN-16cg	V>18.1	20160301	P8	C	80	42
		20160302	P8	C	80	58
		20160303	P8	C	80	72
		20160304	P8	C	80	76
ASASSN-16cq	g=22.7	20160307	0.5m-TNO	V	20	330
		20160308	0.5m-TNO	V	20	426
		20160310	0.5m-TNO	V	50	165
		20160311	0.5m-TNO	V	50	167
		20160312	0.5m-TNO	V	50	121
		20160313	0.5m-TNO	V	80	110
		20160316	0.5m-TNO	V	110	15
		20160318	0.5m-TNO	V	140	54
ASASSN-16da	g=21.5	20160314	0.5m-TNO	V	110	179
		20160315	0.5m-TNO	V	80	283
		20160316	0.5m-TNO	V	110	169
		20160317	0.5m-TNO	V	110	162
		20160318	0.5m-TNO	V	140	175
		20160319	0.5m-TNO	V	140	110
ASASSN-16er	no match	20160426	0.5m-TNO	V	30	274
		20160427	0.5m-TNO	V	20	271
		20160427	P8	C	30	58
ASASSN-16ez	g=21.3	20160510	0.5m-TNO	V	20	411
		20160511	0.5m-TNO	V	20	460

Objects	mag	Date	Telescope	Filter	Exp. (s)	No.
		20160512	0.5m-TNO	V	20	270
		20160513	0.5m-TNO	V	30	291
		20160514	0.5m-TNO	V	30	325
ASASSN-16fi	no match	20160520	P8	C	80	34
		20160521	P8	C	80	123
ASASSN-16fu	g=21.6	20160609	P8	V	30	227
		20160610	P8	V	30	262
		20160611	P8	V	30	219
		20160615	P8	V	30	67
		20160616	P8	V	30	285
		20160618	P8	V	30	229
		20160619	P8	V	30	300
ASASSN-16gh	no match	20160620	P8	V	20	115
		20160621	P8	C	20	176
		20160622	P8	C	30	5
		20160623	P8	C	30	175
		20160627	P8	C	60	98
		20160628	P8	C	60	203
		20160629	P8	C	60	200
ASASSN-16lf	20.2	20161006	P8	C	30	122
		20161007	P8	C	30	300
		20161008	P8	C	30	136
		20161009	P8	C	30	128
		20161010	P8	C	30	204
SDSSJ124043.43+671035.9	g=18.2	20160408	TNT/Uspec	KG5	20	363

2.2 การรีดิวซ์ข้อมูล

การรีดิวซ์ข้อมูล (data reduction) คือการลบสัญญาณที่ไม่ต้องการออกจาก science frames/raw images หรือเป็นการทำให้ภาพ "สะอาด" ขึ้น ซึ่งสัญญาณที่ไม่ต้องการดังกล่าวนั้นเกิดจากโครงสร้างของซีซีดี การรีดิวซ์ข้อมูลทางโฟโตเมตรจากกล้องโทรทรรศน์ 0.5 เมตร ได้ดำเนินการในโปรแกรม MIDAS ซึ่งเป็นโปรแกรมวิเคราะห์ภาพถ่ายทางดาราศาสตร์ขั้นสูง ผ่านชุดคำสั่งในโปรแกรมย่อยที่เขียนขึ้นโดย Gänsicke,B. T. (2004) และการรีดิวซ์ข้อมูลจาก ULTRASPEC ดำเนินการผ่านชุดคำสั่งของ ULTRASPEC ซอร์ฟแวร์ ซึ่งพัฒนาโดยทีม ULTRASPEC การรีดิวซ์ข้อมูลทางโฟโตเมตรีมีขั้นตอนดังต่อไปนี้

1. การลบสัญญาณ bias (bias-subtraction)

โดยทั่วไปในซีซีดี มีสัญญาณทางอิเล็กทรอนิกส์ที่ผู้ผลิตซีซีดี ใส่เพิ่มเข้าไปเพื่อหลีกเลี่ยงค่าที่เป็นลบในระหว่างการแปลงสัญญาณอะนาลอกเป็นดิจิตอลในกระบวนการอ่านข้อมูลของ ซีซีดี (CCD readout) เราสามารถลบระดับของไบแอส (bias level) ออกจากภาพได้โดยการนำเอาค่าเฉลี่ยของไบแอสเฟรม (mean bias frame) ประมาณ 10 ภาพ สำหรับกล้องซีซีดีทั่วไป และประมาณ 50 ภาพ สำหรับ USPEC มาลบออกจาก ภาพข้อมูล ซึ่งการถ่ายไบแอส เป็นการถ่ายภาพโดยการปิดชัตเตอร์และใช้เวลาในการถ่าย 0 วินาที หรือเป็นการอ่านค่าสัญญาณทางอิเล็กทรอนิกส์ในกระบวนการอ่านข้อมูลของซีซีดี

2. การลบ "กระแสมืด" (dark current-subtraction)

โดยทั่วไปในซีซีดี ที่ไม่มีการหล่อเย็นด้วยไนโตรเจนเหลวจะมีความร้อนเกิดขึ้นได้ง่าย อิเล็กตรอนที่เกิดจากความร้อนในซีซีดี เป็นสาเหตุให้เกิด "กระแสมืด" ซึ่งเป็นสัญญาณรบกวนที่ทำให้ภาพถ่ายซีซีดี "สกปรก" โดยที่จำนวนอิเล็กตรอนที่เกิดจากความร้อนในซีซีดี เป็นสัดส่วนโดยตรงกับเวลาที่ใช้ในการเปิดหน้ากล้องขณะทำการเก็บข้อมูล ดังนั้นเพื่อที่จะลบกระแสมืดเราต้องทำการถ่ายดาร์กเฟรม โดยการปิดชัตเตอร์ และใช้เวลาในการเปิดหน้ากล้องเท่ากับเวลาที่ใช้ในการเก็บข้อมูล ประมาณ 10 ภาพ เพื่อนำมาหาดาร์กเฟรมเฉลี่ย (mean dark frame) และนำภาพดังกล่าวไปลบออกจากภาพข้อมูล

3. การทำ flat-fielding

เนื่องจากซีซีดี แต่ละพิกเซล มีความไวต่อการรับแสงไม่เท่ากัน ทั้งนี้อาจเนื่องมาจากกระบวนการผลิตซีซีดี หรืออาจเกิดจากการสะสมของฝุ่นบนกระจกและเลนส์ของกล้อง หรือในตัวซีซีดีเอง ในทางปฏิบัติเราสามารถ "ปรับ" ให้ซีซีดี แต่ละพิกเซลมีความสามารถในการรับแสงเท่ากันได้ โดยการถ่ายภาพบริเวณที่แสงมีการกระจายตัวแบบสม่ำเสมอ เช่น ท้องฟ้า หรือ sky flat-field โดยใช้แผ่นกรองแสงหรือฟิลเตอร์เดียวกันกับการเก็บข้อมูล ประมาณ 10 ภาพ เพื่อหาแฟลตฟิลด์เฟรมเฉลี่ย (mean flat-field frame) และนำภาพดังกล่าวไปหารภาพข้อมูล ที่ลบระดับไบแอสและกระแสมืดเรียบร้อยแล้ว ตามสมการ

$$\text{Reduced images} = \frac{\text{Raw images} - \text{mean bias} - \text{mean dark}}{\text{Mean flat fields}}$$

บทที่ 3
การวิเคราะห์ข้อมูล

3.1 การสร้างกราฟแสง

การจะนำข้อมูลทางดาราศาสตร์ที่อยู่ในภาพที่รีดิวซ์แล้วมาใช้ประโยชน์นั้น เราจำเป็นต้อง "สกัด" (extract) หรือวัดปริมาณแสงดาวแต่ละดวงที่อยู่ในภาพ หรือทำโฟโตเมตรีของดาวแต่ละดวงนั่นเอง ซึ่งในงานวิจัยนี้ใช้ Bertin's SExtractor (1996) โดยปริมาณที่วัดได้จะอยู่ในรูปของแมกนิจูดเครื่องมือ (instrumental magnitude) เราสร้างกราฟแสงของ CVs จากการทำดิฟเฟอเรนเชียลโฟโตเมตรี ซึ่งเป็นเทคนิคการวัดความสว่างของวัตถุเทียบกับความสว่างของดาวเปรียบเทียบและดาวตรวจสอบ โดยผลที่ได้จะอยู่ในรูปของผลต่างแมกนิจูด (Δm) ตามสมการ

$$\Delta m = m_{target} - m_{C_1}$$

เมื่อ m_{target} = แมกนิจูดปรากฏของวัตถุ

m_{C_1} = แมกนิจูดปรากฏของดาวเปรียบเทียบ

โดยที่

$$m_{C_1} - m_{C_2} = \text{คงที่}$$

เมื่อ m_{C_2} = แมกนิจูดของดาวตรวจสอบ

รูปที่ 1-16 แสดงกราฟแสงที่ได้จากการสังเกตของระบบที่แสดงในตารางที่ 1 และรายละเอียดของกราฟแสง แสดงในตารางที่ 2

ตารางที่ 2 รายละเอียดของกราฟแสง

Objects	Comments on Light curves
CSS150211:091017-200813	Superhump structure with the strongest peak at 48.523 d^{-1} or Psh = 29.67 min
ASASSN-15sz	Superhump structure with the strongest peak at 38.369 d^{-1} or Psh = 37.53 min
ASASSN-16bf	1 mag variation with a possible period at 10.11 d^{-1} or 142 min
ASASSN-16bh	Superhump structure with the strongest signal at 18.23 d^{-1} or Psh = 78.99 min
ASASSN-16bi	Superhump structure with the strongest signal at 17.18 d^{-1} or Psh = 83.8 min
ASASSN-16by	0.1 mag variation with no sign of superhump structure
ASASSN-16cg	0.1 mag variation with no sign of superhump structure
ASASSN-16cq	Superhump structure with the strongest signal at 16.86 d^{-1} or Psh = 85.4 min
ASASSN-16da	Superhump structure with the strongest signal at 17.46 d^{-1} or Psh = 82.5 min
ASASSN-16er	Small variation of 0.2 mag with a sign of variation at 21.20 d^{-1}
ASASSN-16ez	Superhump structure with the strongest signal at 17.36 d^{-1} or Psh = 82.9 min
ASASSN-16fi	0.6 mag variation with no sign of superhump structure
ASASSN-16fu	Superhump structure with the strongest signal at 17.57 d^{-1} or Psh = 81.96 min
ASASSN-16gh	Superhump structure with the strongest signal at 15.64 d^{-1} or Psh = 92.06 min
ASASSN-16lf	Superhump structure with the strongest signal at 16.04 d^{-1} or Psh = 89.76 min
SDSSJ124043.43+671035.9	Flat light curve with 0.2 mag variation

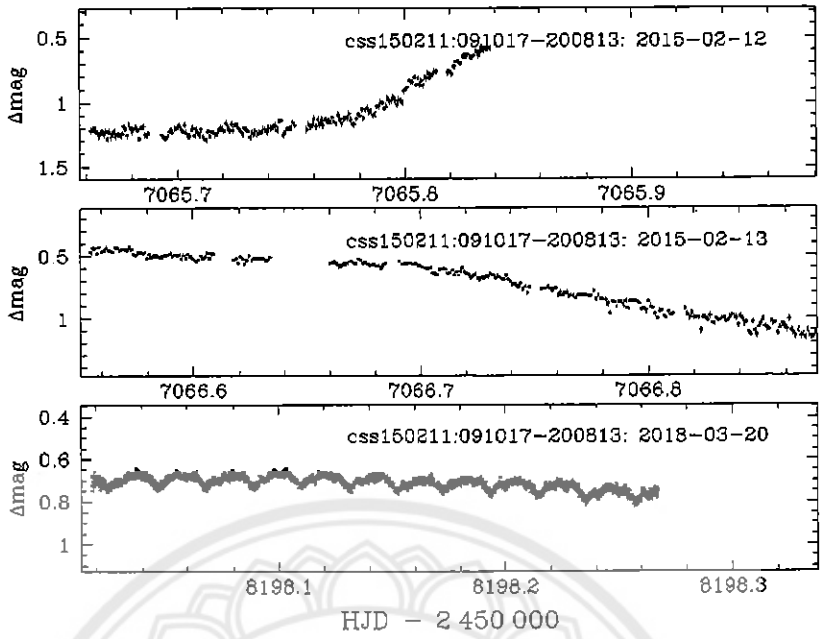

รูปที่ 1 กราฟแสงของ CSS150211:091017-200813

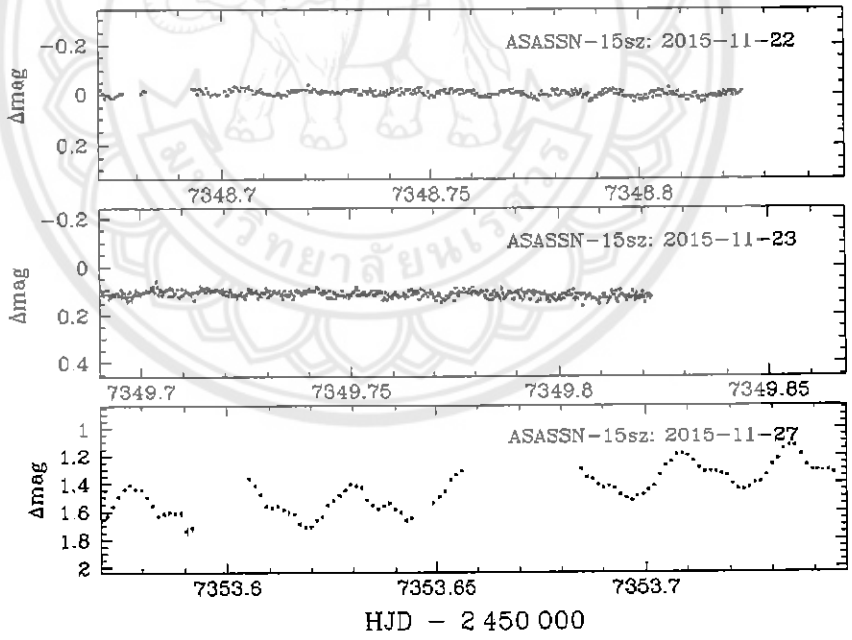

รูปที่ 2 กราฟแสงของ ASASSN-15sz

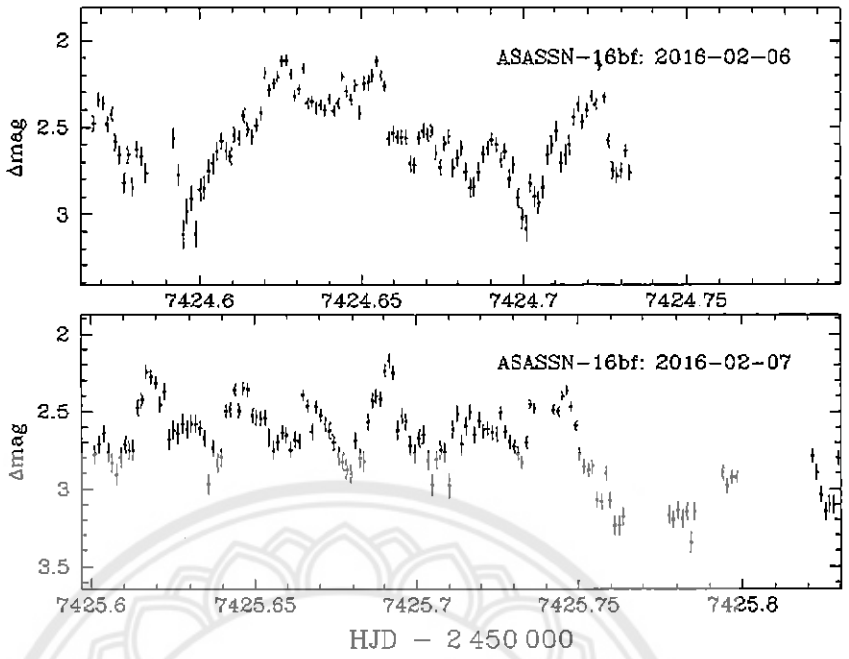

รูปที่ 3 กราฟแสงของ ASASSN-16bf

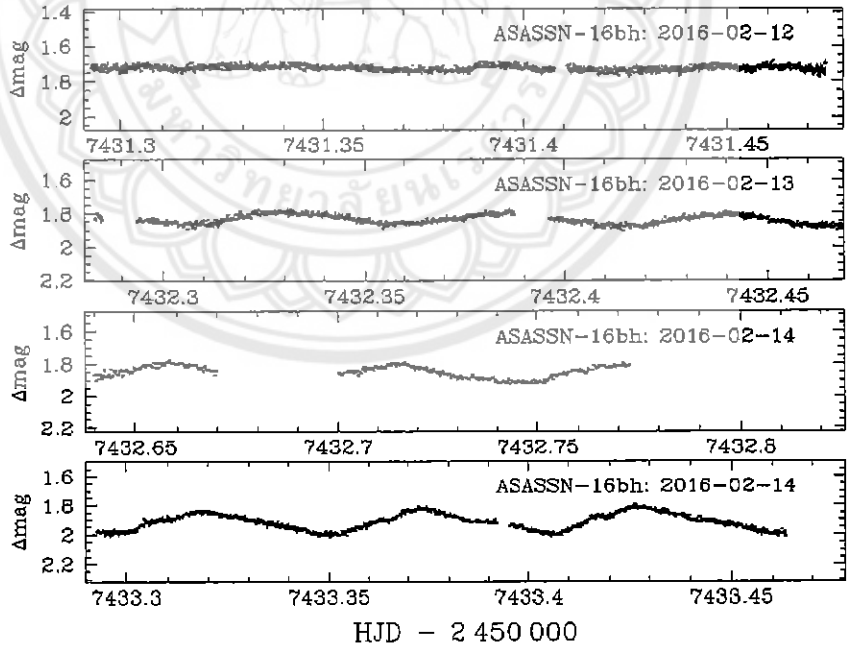

รูปที่ 4 กราฟแสงของ ASASSN-16bh

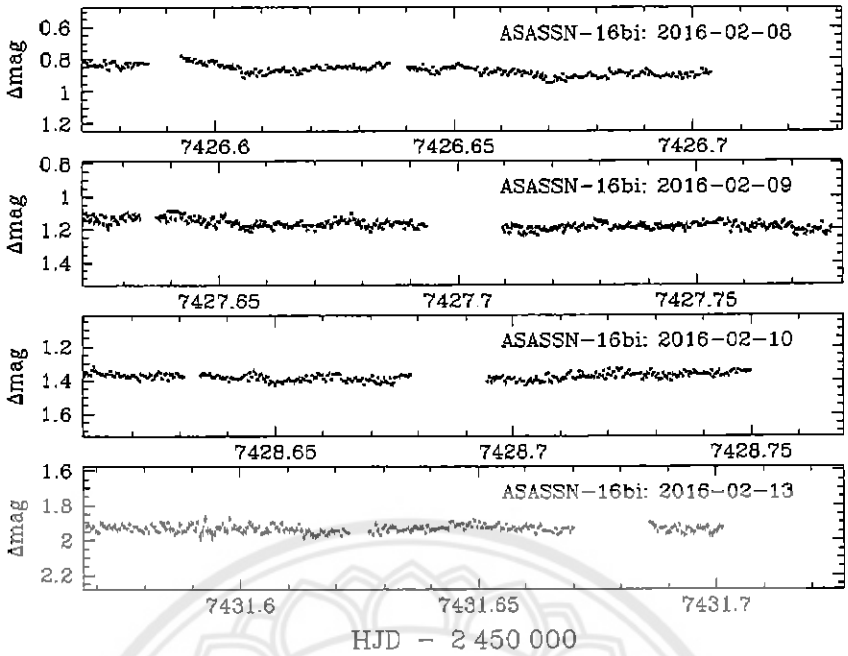

รูปที่ 5 กราฟแสงของ ASASSN-16bi

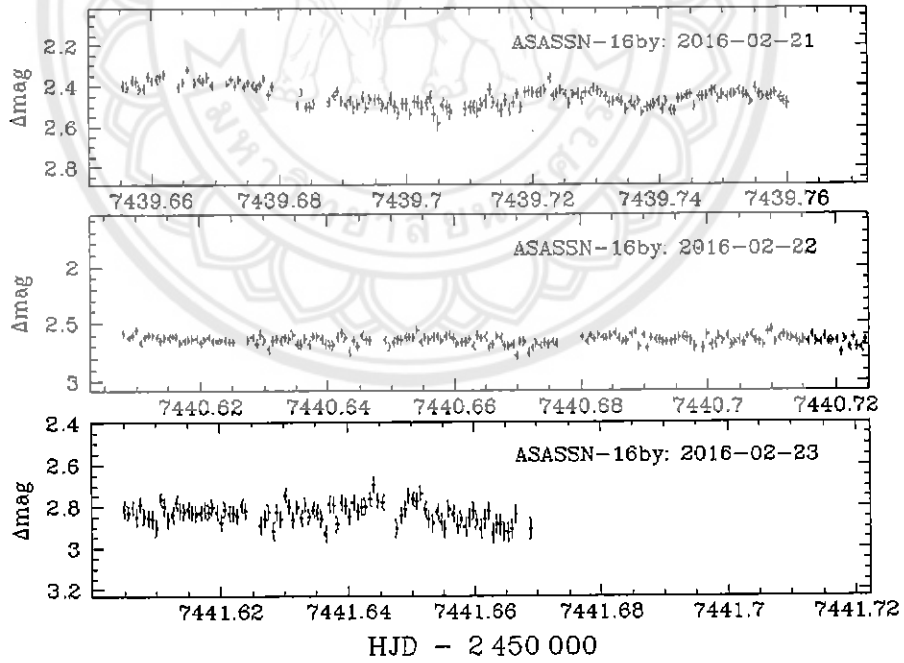

รูปที่ 6 กราฟแสงของ ASASSN-16by

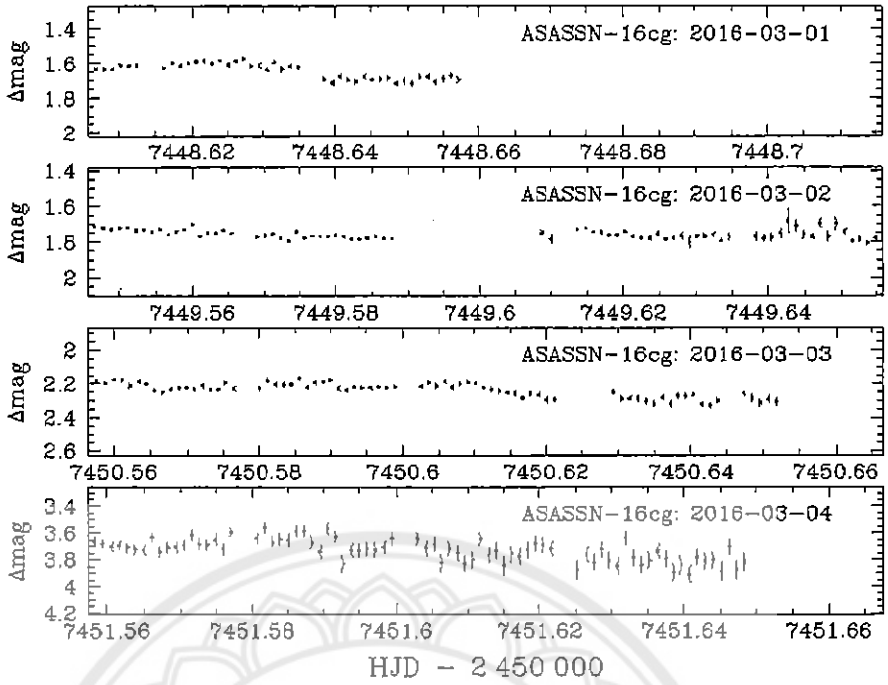

รูปที่ 7 กราฟแสงของ ASASSN-16cg

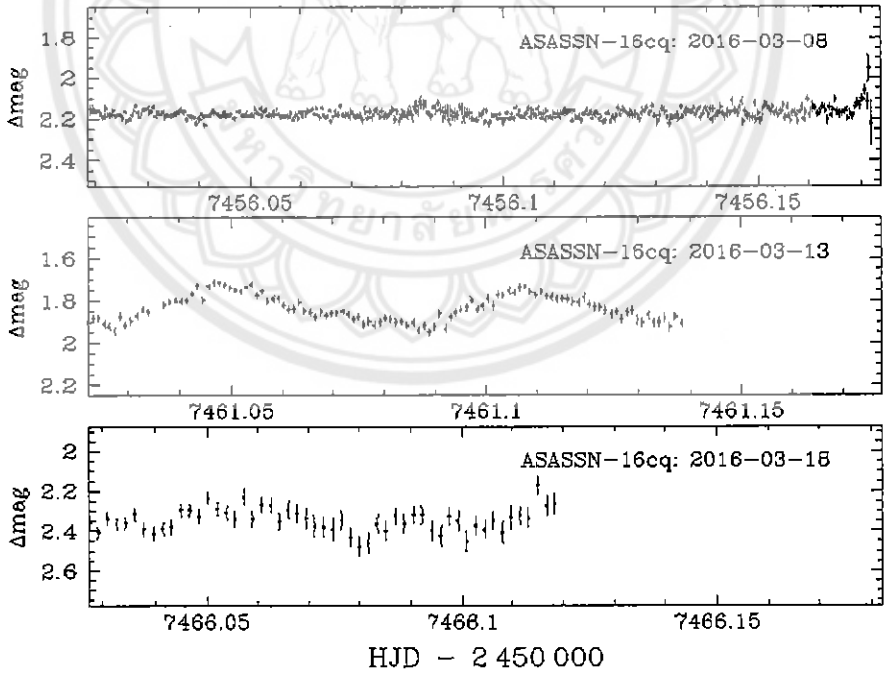

รูปที่ 8 กราฟแสงของ ASASSN-16cq

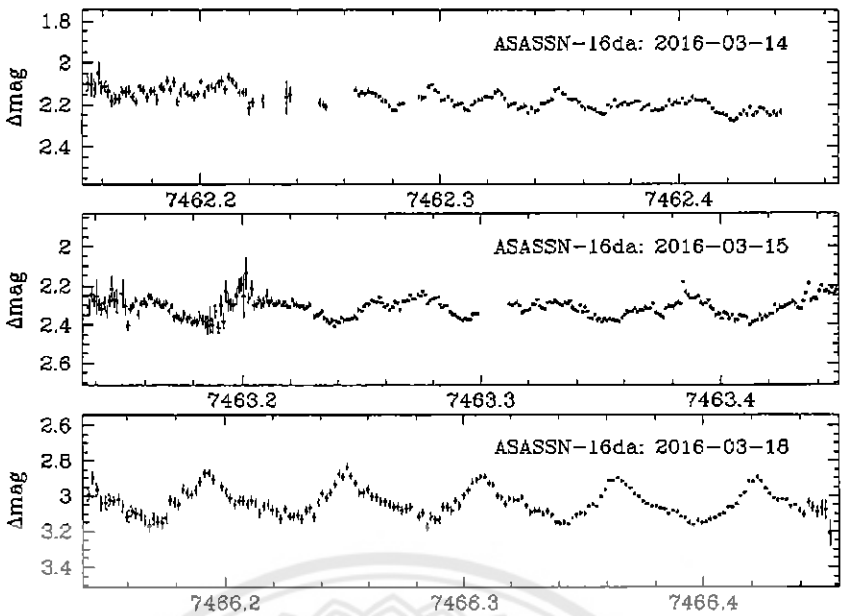

รูปที่ 9 กราฟแสงของ ASASSN-16da

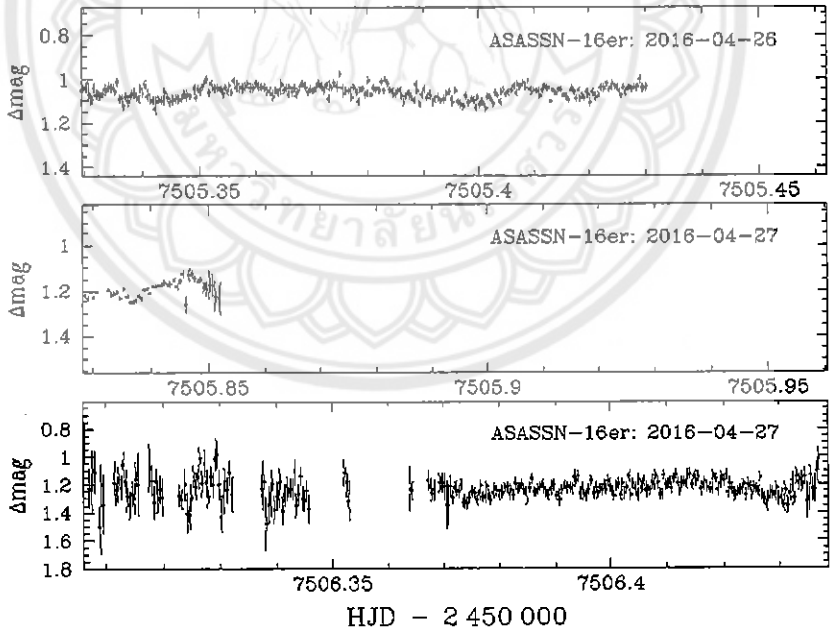

รูปที่ 10 กราฟแสงของ ASASSN-16er

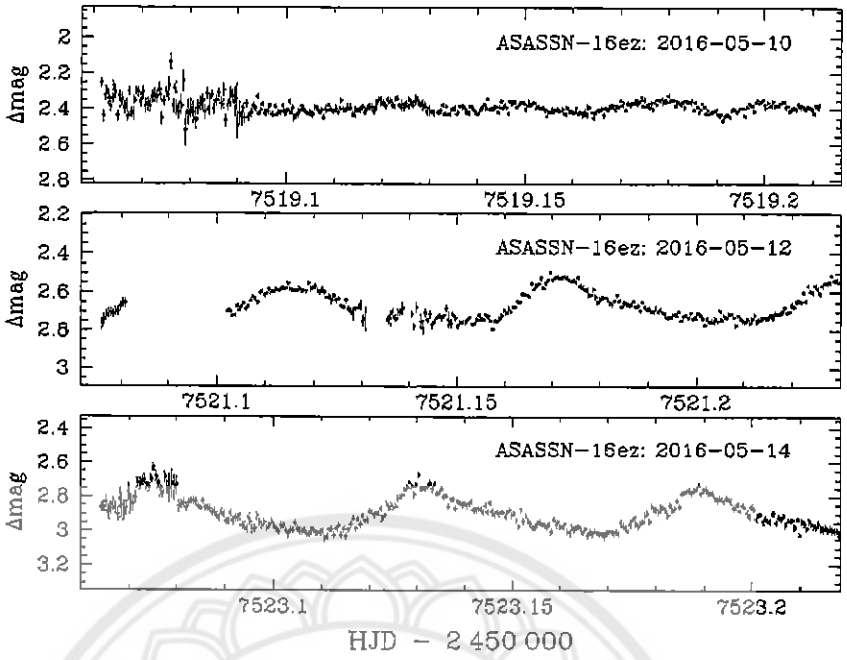

รูปที่ 11 กราฟแสงของ ASASSN-16ez

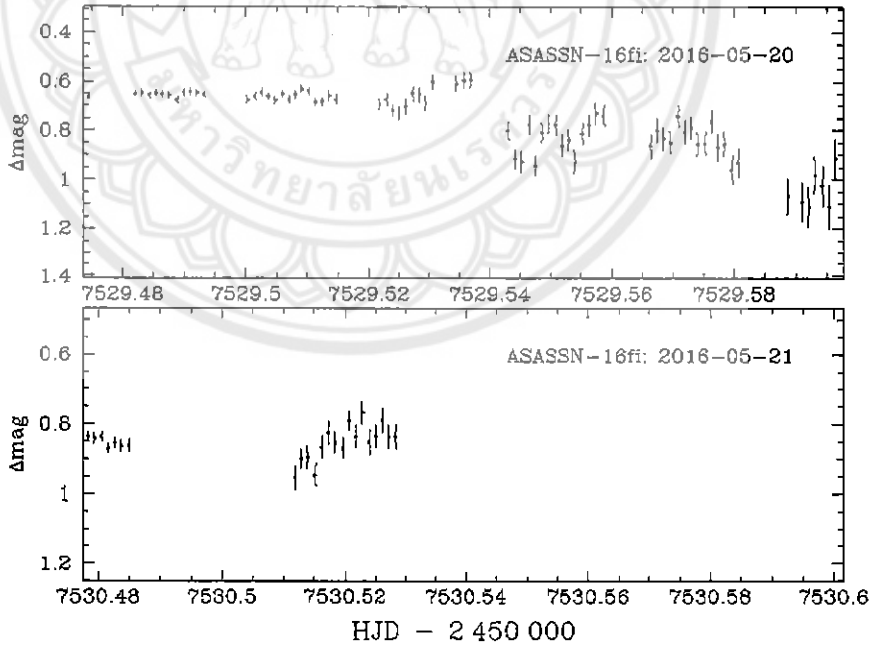

รูปที่ 12 กราฟแสงของ ASASSN-16fi

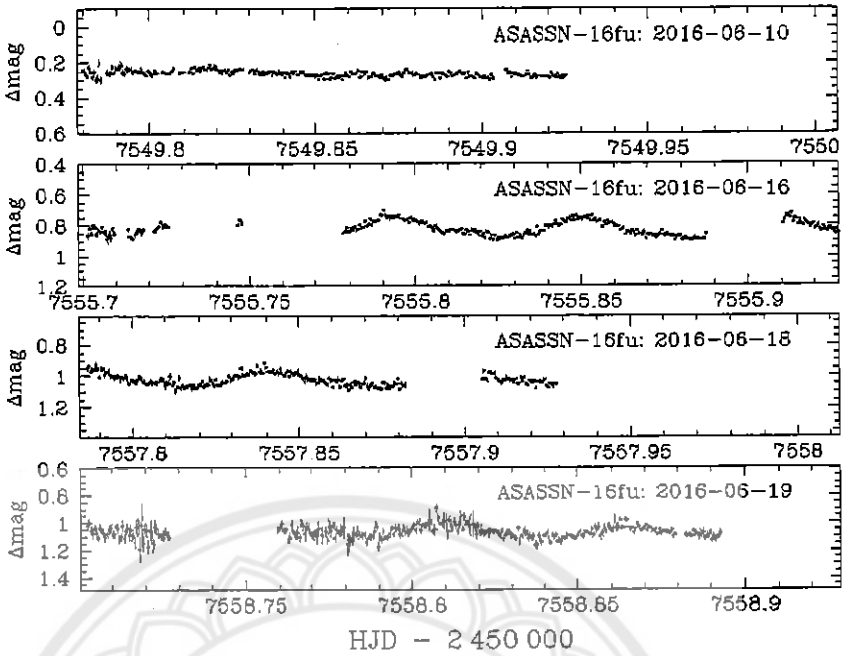

รูปที่ 13 กราฟแสงของ ASASSN-16fu

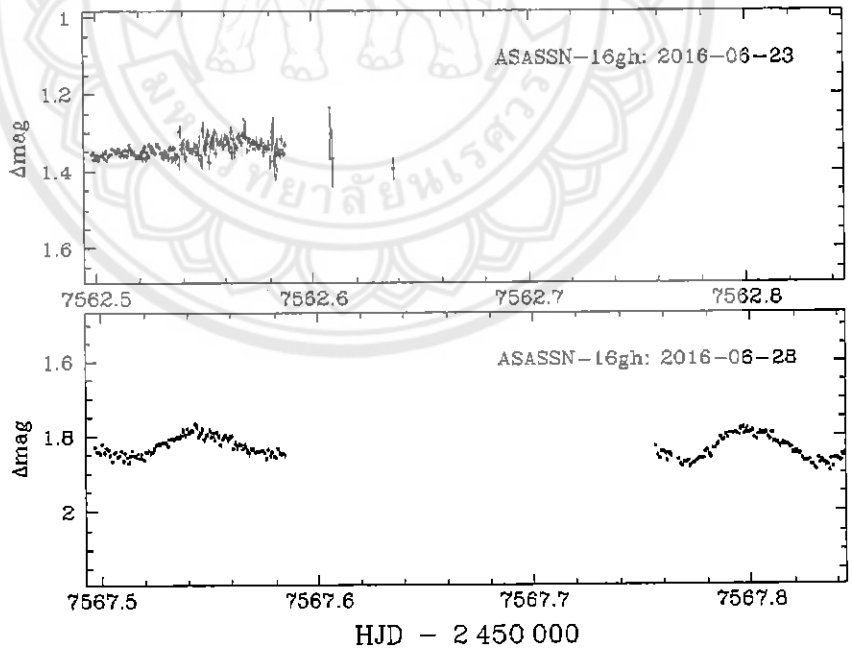

รูปที่ 14 กราฟแสงของ ASASSN-16gh

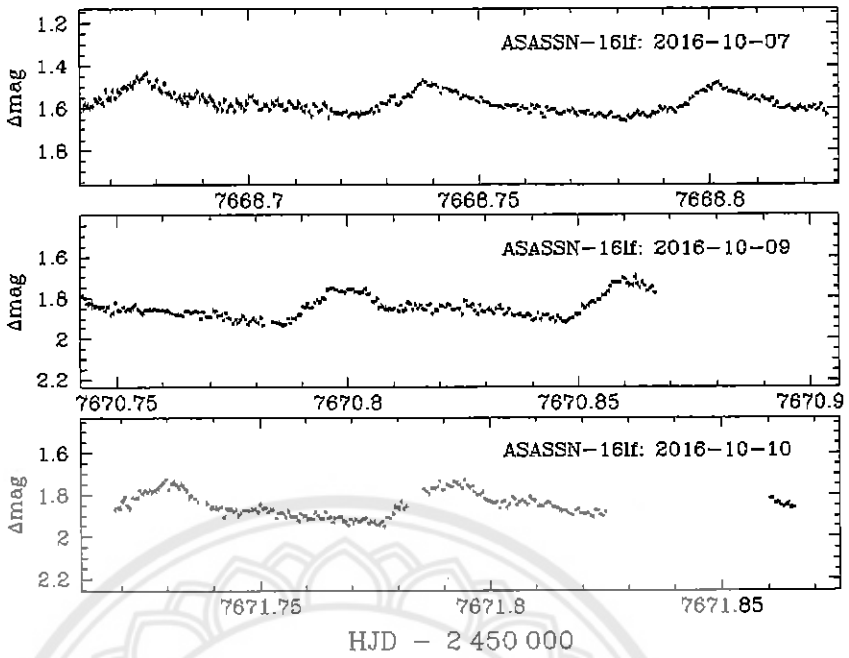

รูปที่ 15 กราฟแสงของ ASASSN-16lt

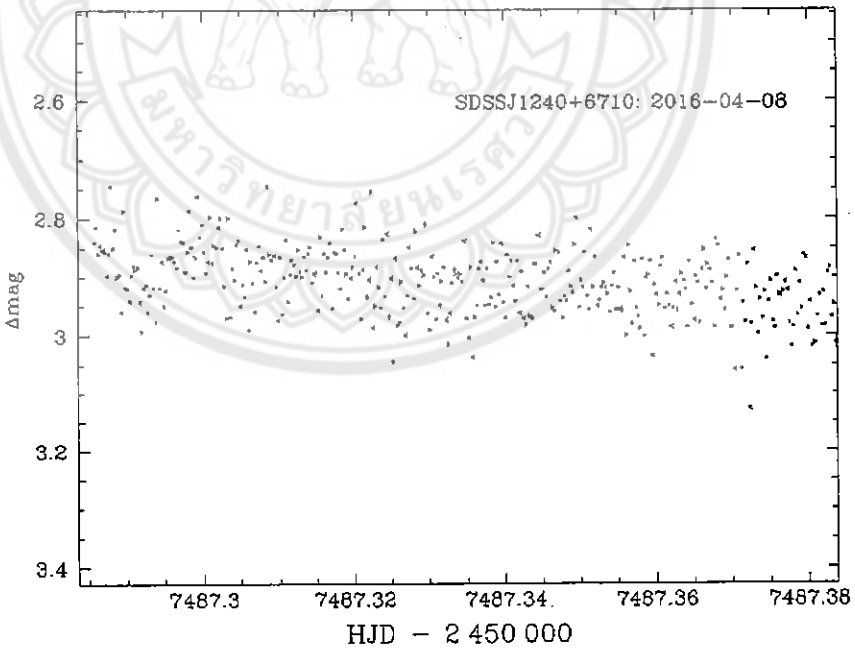

รูปที่ 16 กราฟแสงของ SDSSJ124043.43+671035.9

3.2 การวิเคราะห์กราฟแสง

เพื่อที่จะวัดคาบการโคจรของระบบและคาบ superhump จากการระเบิดใหญ่ ซึ่งสัมพันธ์กับคาบการโคจรของระบบ เราทำการวิเคราะห์กราฟแสงของ CVs ในตารางที่ 1 โดยใช้เทคนิคการวิเคราะห์อนุกรมเวลา (time-series analysis) จากโปรแกรมย่อย Time-Series Analysis ใน MIDAS (MIDAS/TSA package) ที่เขียนโดย A.Schwarzenberg-Czerny โดยใช้วิธีการวิเคราะห์แบบฟูเรียร์ (Fourier analysis) ภายใต้บริบท Scargle/TSA สร้างโดย Scargle ซึ่งเป็นวิธีที่เหมาะสำหรับการวิเคราะห์หาคาบการโคจรของระบบที่ให้สัญญาณที่มีการแปรค่าแบบราบเรียบ เช่น สัญญาณรูปไซน์ (sinusoidal signals)

รูปที่ 17--32 แสดง periodogram ที่คำนวณจากกราฟแสงของแต่ละระบบ และการนำข้อมูลทางโฟโตเมตรีที่ได้จากการสังเกตการณ์มาพล็อตในรูปของเฟสการโคจร (phase folded) โดยใช้ความถี่ของพีคสูงสุดของสัญญาณที่ได้จาก periodogram ตารางที่ 2 แสดงรายละเอียดของกราฟแสงและคาบการโคจร (Porb)/คาบ superhump (Psh) ของระบบ

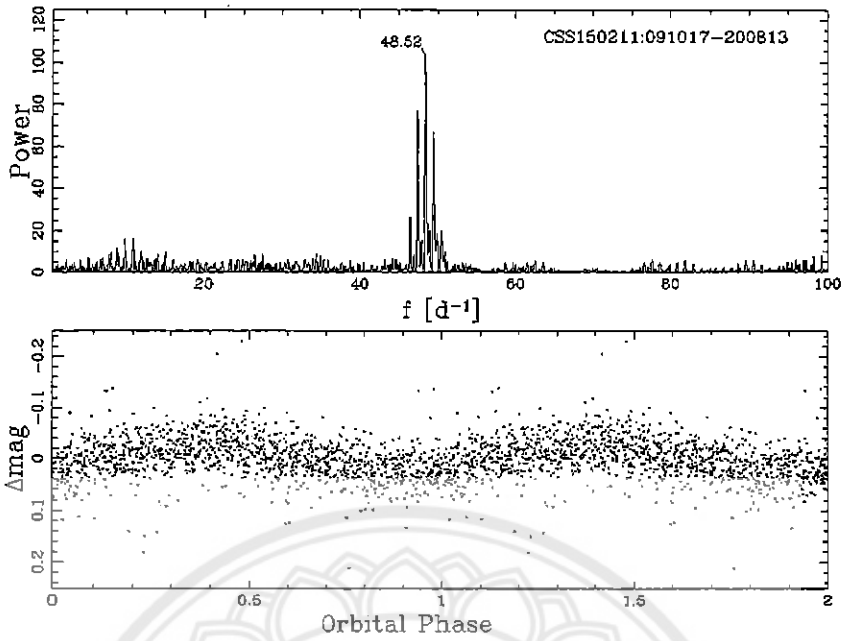

รูปที่ 17 Scargle periodogram และ phase folded ของ CSS150211:091017-200813

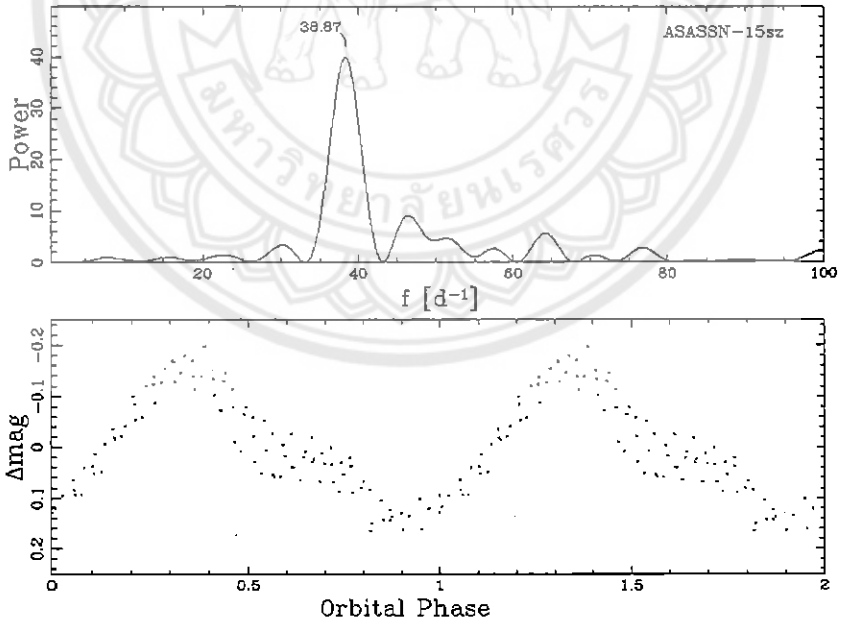

รูปที่ 18 Scargle periodogram และ phase folded ของ ASASSN-15sz

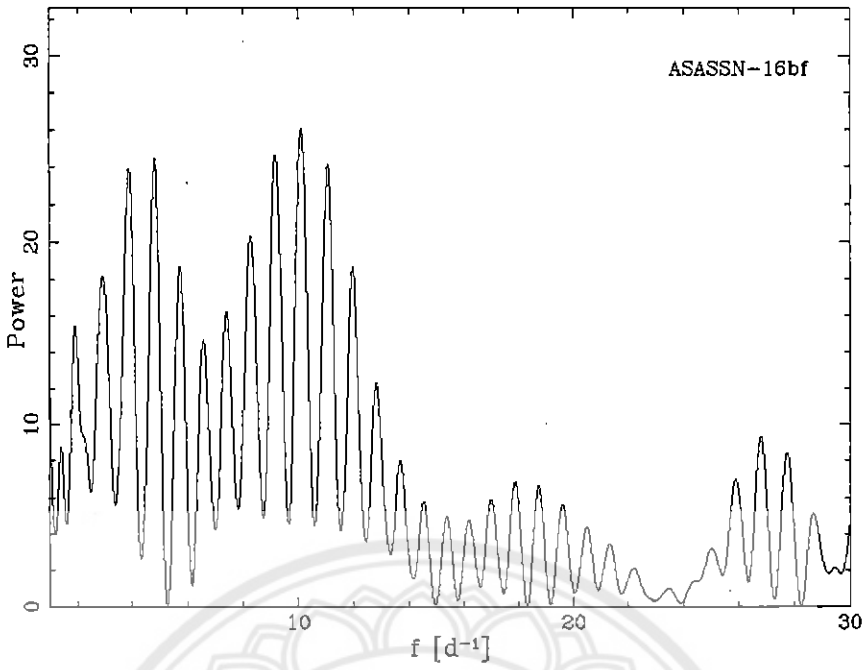

รูปที่ 19 Scargle periodogram ของ ASASSN-16bf

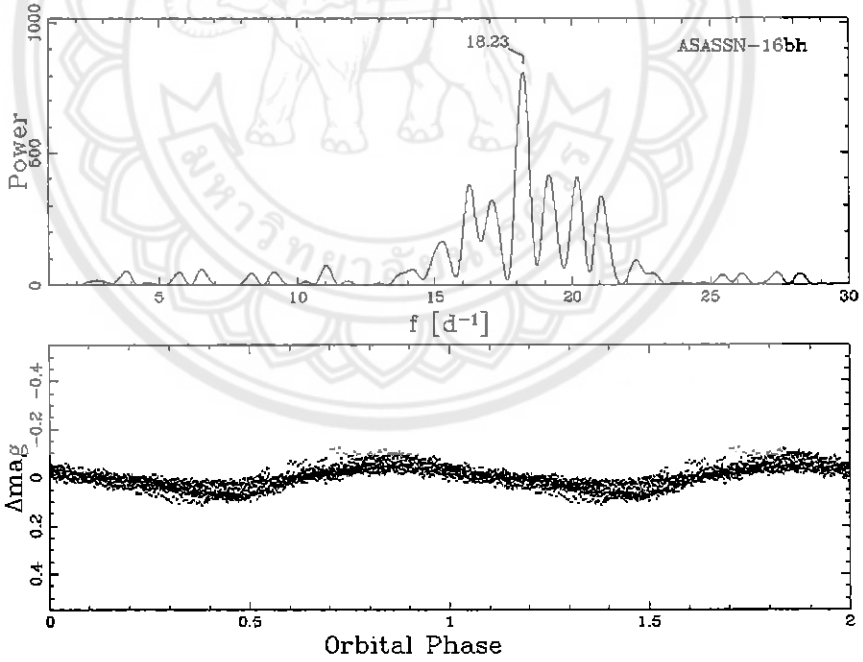

รูปที่ 20 Scargle periodogram และ phase folded ของ ASASSN-16bh

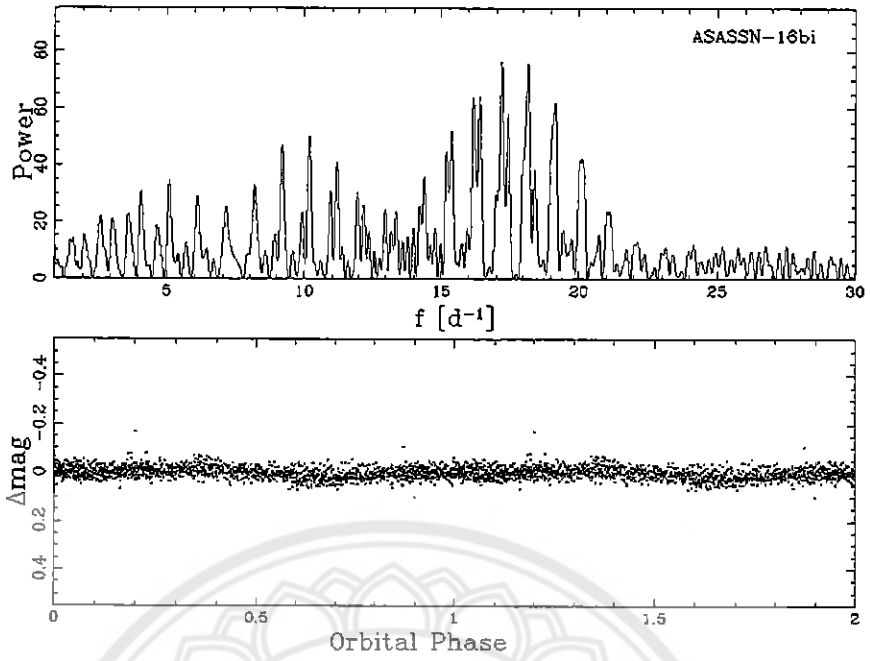

รูปที่ 21 Scargle periodogram และ phase folded ของ ASASSN-16bi

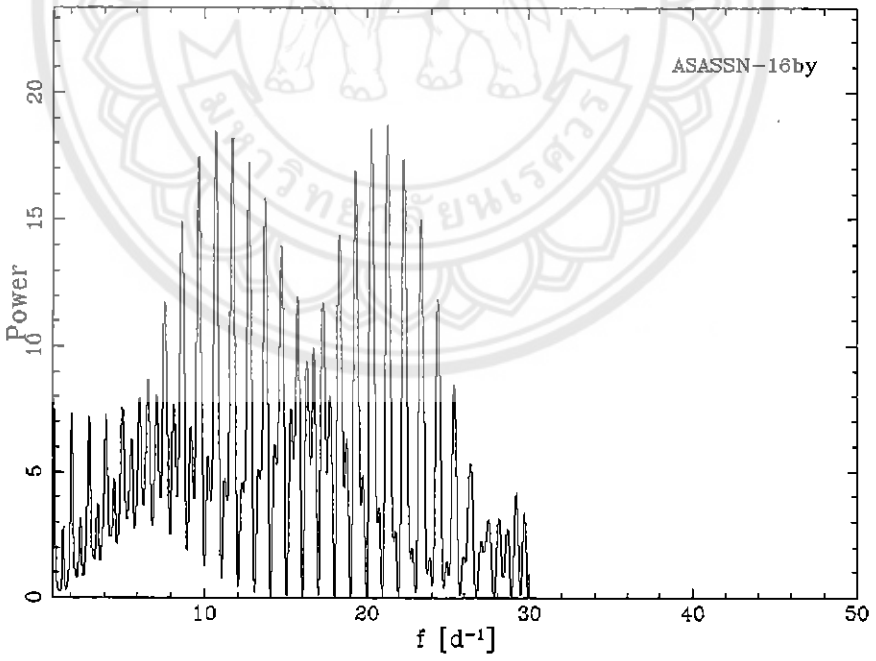

รูปที่ 22 Scargle periodogram ของ ASASSN-16by

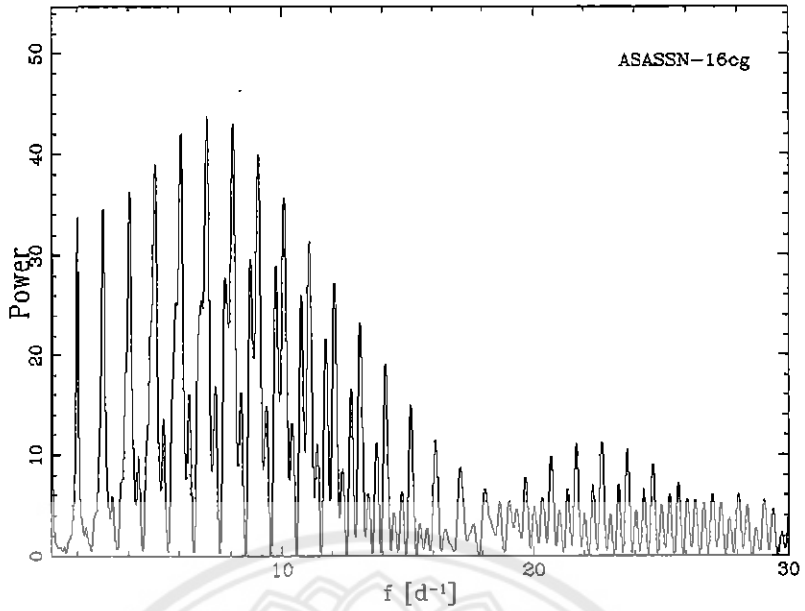

รูปที่ 23 Scargle periodogram ของ ASASSN-16cg

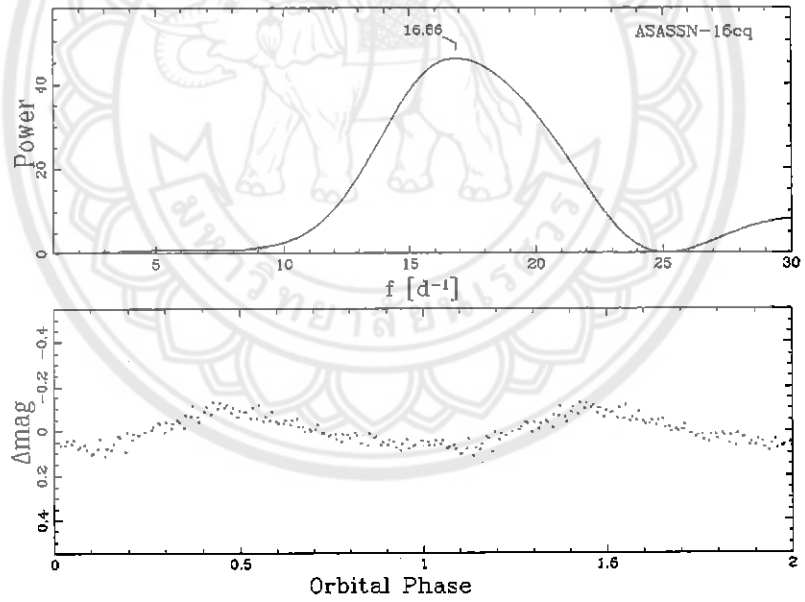

รูปที่ 24 Scargle periodogram และ phase folded ของ ASASSN-16cq

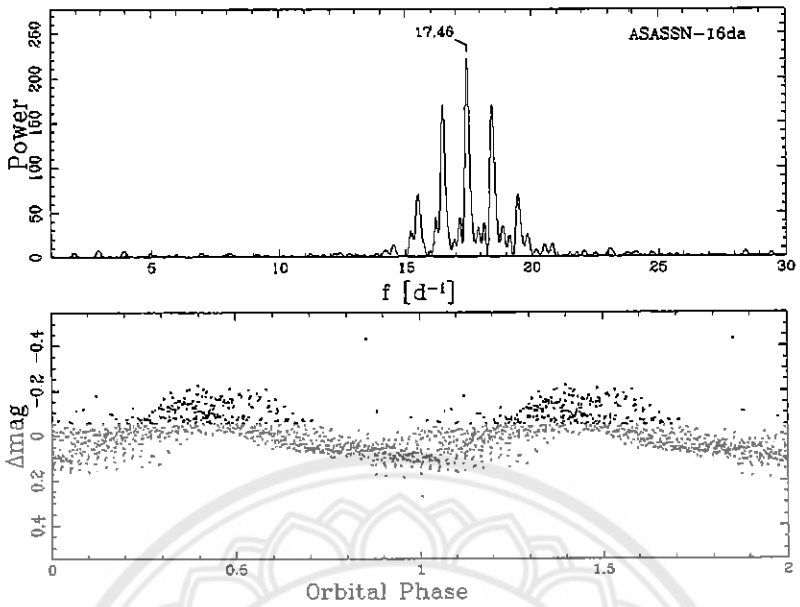

รูปที่ 25 Scargle periodogram และ phase folded ของ ASASSN-16da

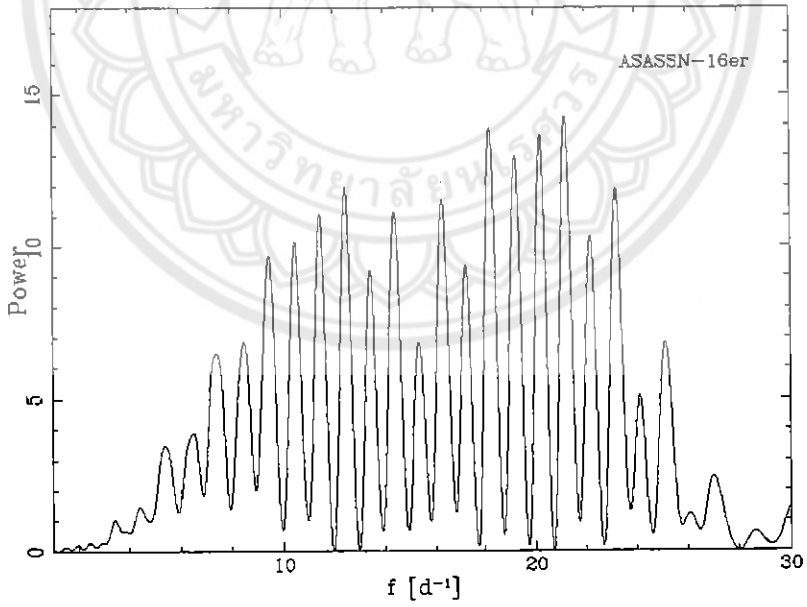

รูปที่ 26 Scargle periodogram ของ ASASSN-16er

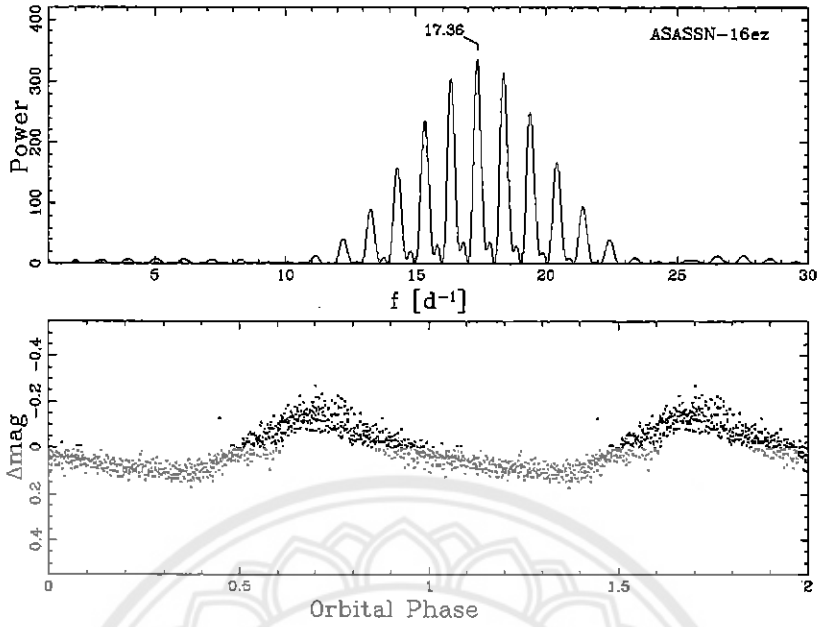

รูปที่ 27 Scargle periodogram และ phase folded ของ ASASSN-16ez

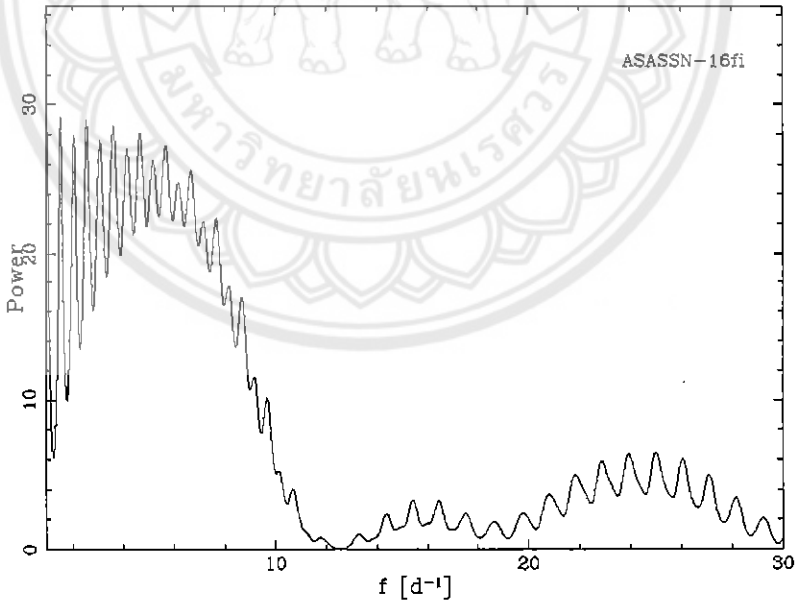

รูปที่ 28 Scargle periodogram ของ ASASSN-16fi

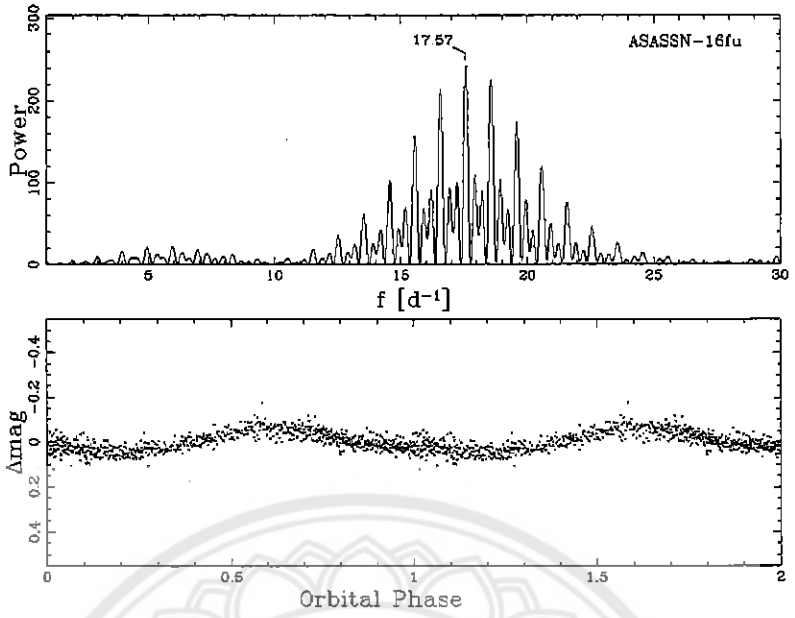

รูปที่ 29 Scargle periodogram และ phase folded ของ ASASSN-16fu

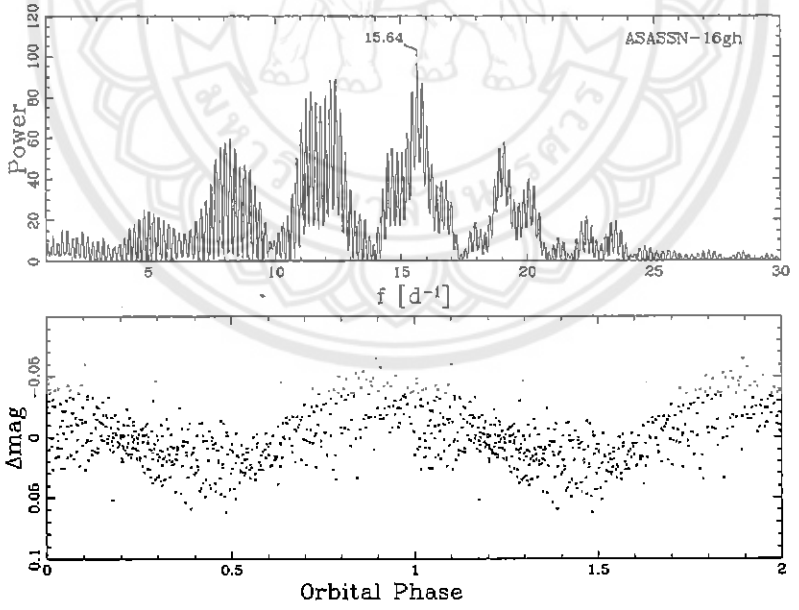

รูปที่ 30 Scargle periodogram และ phase folded ของ ASASSN-16gh

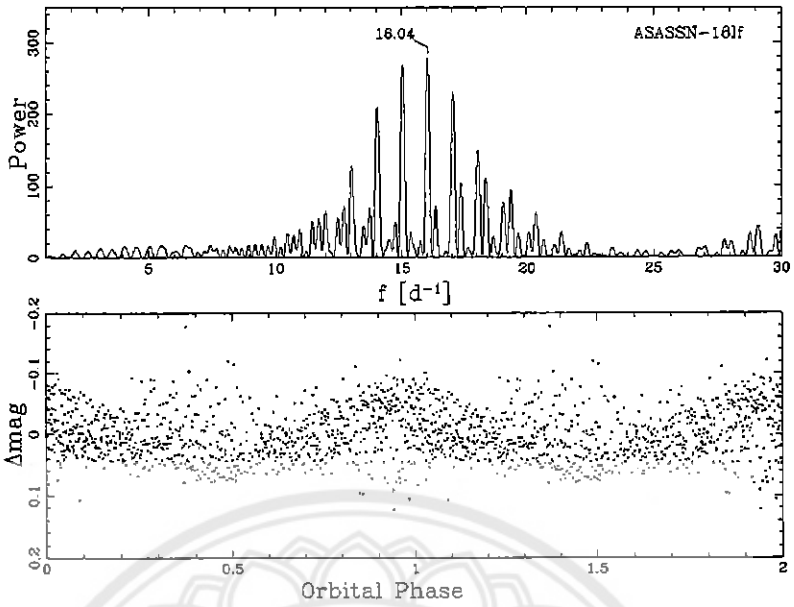

รูปที่ 31 Scargle periodogram และ phase folded ของ ASASSN-16lf

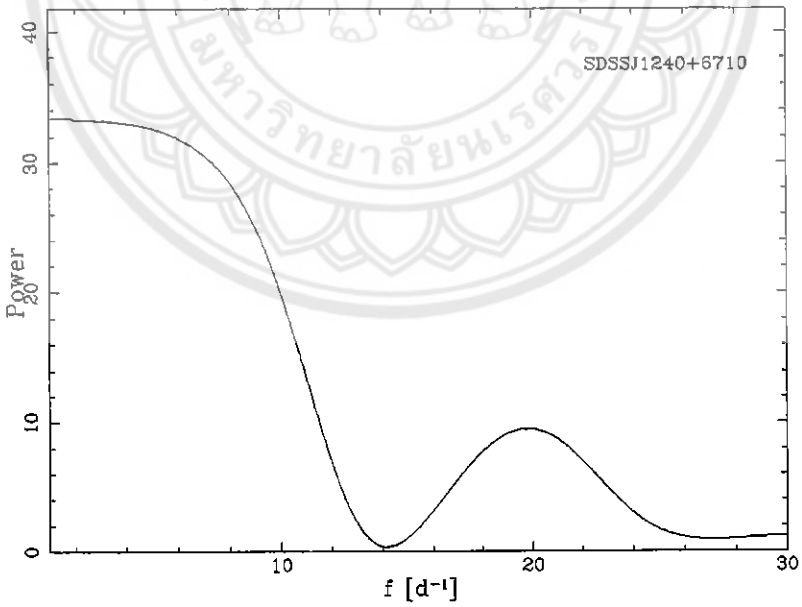

รูปที่ 32 Scargle periodogram ของ SDSSJ124043.43+671035.9

บทที่ 4
สรุป

งานวิจัยนี้ทำการค้นหา CVs คาบการโคจรสั้นระบบใหม่ๆ จากสมบัติทางการระเบิดใหญ่ ซึ่งตรวจพบเซอร์เวย์ขนาดใหญ่ เช่น CRTS, ASASSN ที่อยู่ในพื้นที่เดียวกับ SDSS เพื่อวัดคาบการโคจรและ superhump ของระบบ โดยทั่วไปคาบ superhump สัมพันธ์กับคาบการโคจรของระบบ กล่าวคือ คาบ superhump ขณะเกิดการระเบิดใหญ่จะมีค่ามากกว่าคาบการโคจรของระบบเล็กน้อย (ประมาณ 3-5 นาที) เนื่องจากโครงสร้างที่บิดเบี้ยวของ superhump ซึ่งเกิดจากการส่ายของมวลสารใน accretion disc เราเก็บข้อมูลอนุกรมเวลาทางโฟโตเมตรีของ CV candidates จำนวน 16 ระบบ และวัดคาบ superhump (Psh) ของ CVs ทั้งหมดจำนวน 8 ระบบ ซึ่งมี $P_{sh} < 2$ ชั่วโมง โดยมีรายละเอียดดังนี้ ASASSN-16bi (Psh = 83.8 นาที), ASASSN-16cq (Psh = 85.4 นาที), ASASSN-16da (Psh = 82.5 นาที), ASASSN-16ez (Psh = 82.9 นาที), ASASSN-16fu (Psh = 81.96 นาที), ASASSN-16gh (Psh = 92.06 นาที), ASASSN-16lf (Psh = 89.76 นาที) และ ASASSN-16bh มีคาบ superhump ประมาณ ค่าคาบการโคจรที่น้อยที่สุด (period minimum) ของ CVs (Psh = 78.99 นาที) เนื่องจากกราฟแสงของ CVs เหล่านี้แสดงให้เห็นโครงสร้าง superhump อย่างชัดเจน เราจึงจำแนกประเภทระบบเหล่านี้เป็น SU UMa dwarf novae

นอกจากนี้เรายังค้นพบ AM CVn ซึ่งอาจเป็นขั้นตอนสุดท้ายของ CVs จำนวน 2 ระบบ โดยมีคาบ superhump ดังนี้ CSS150211:091017-200813 (Psh = 29.67 นาที) และ ASASSN-15sz (Psh = 37.53 นาที)

Output

- **ผลงานวิจัยที่ได้รับการตีพิมพ์ในวารสารวิชาการระดับนานาชาติ**

1. Ramsay, G., Green, M. J., Marsh, T. R., Kupfer, T., Breedt, E., Korol, V., Groot, P. J., Knigge, C., Nelemans, G., Steeghs, D., Woudt, P., **Aungwerojwit, A.,** "The physical properties of AM CVn stars: new insights from Gaia DR2" *Astronomy & Astrophysics*, 2018, Volume 620, id. A141, 17 pp. (Q1, IF = 5.565)

ภาคผนวก

A&A 620, A141 (2018)
https://doi.org/10.1051/0004-6361/201834261

Astronomy & Astrophysics

Physical properties of AM CVn stars: New insights from *Gaia* DR2*

G. Ramsay[1], M. J. Green[2], T. R. Marsh[2], T. Kupfer[3,4,5], E. Breedt[6], V. Korol[7], P. J. Groot[8], C. Knigge[9], G. Nelemans[8,10], D. Steeghs[2], P. Woudt[11], and A. Aungwerojwit[12]

[1] Armagh Observatory and Planetarium, College Hill. Armagh BT61 9DG, UK
e-mail: gavin.ramsay@armagh.ac.uk
[2] Department of Physics, University of Warwick, Coventry CV4 7AL, UK
[3] Kavli Institute for Theoretical Physics, University of California, Santa Barbara, CA 93106, USA
[4] Department of Physics, University of California, Santa Barbara, CA 93106, USA
[5] Division of Physics, Mathematics and Astronomy, California Institute of Technology, Pasadena, CA 91125, USA
[6] Institute of Astronomy, University of Cambridge, Madingley Road, Cambridge CB3 0HA, UK
[7] Leiden Observatory, Leiden University, PO Box 9513 2300 RA, Leiden, The Netherlands
[8] Department of Astrophysics/IMAPP, Radboud University, PO Box 9010, 6500 GL Nijmegen, The Netherlands
[9] Department of Physics and Astronomy, University of Southampton, Southampton SO17 1BJ, UK
[10] Institute of Astronomy, KU Leuven, Celestijnenlaan 200D, 3001 Leuven, Belgium
[11] Inter-University Institute for Data Intensive Astronomy, Department of Astronomy, University of Cape Town, Private Bag X3 Rondebosch 7701, South Africa
[12] Department of Physics, Faculty of Science, Naresuan University, Phitsanulok 65000, Thailand

Received 17 September 2018 / Accepted 14 October 2018

ABSTRACT

AM CVn binaries are hydrogen deficient compact binaries with an orbital period in the 5–65 min range and are predicted to be strong sources of persistent gravitational wave radiation. Using *Gaia* Data Release 2, we present the parallaxes and proper motions of 41 out of the 56 known systems. Compared to the parallax determined using the HST Fine Guidance Sensor we find that the archetype star, AM CVn, is significantly closer than previously thought. This resolves the high luminosity and mass accretion rate which models had difficulty in explaining. Using Pan-STARRS1 data we determine the absolute magnitude of the AM CVn stars. There is some evidence that donor stars have a higher mass and radius than expected for white dwarfs or that the donors are not white dwarfs. Using the distances to the known AM CVn stars we find strong evidence that a large population of AM CVn stars has yet to be discovered. As this value sets the background to the gravitational wave signal of LISA this is of wide interest. We determine the mass transfer rate for 15 AM CVn stars and find that the majority has a rate significantly greater than expected from standard models. This is further evidence that the donor star has a greater size than expected.

Key words. accretion, accretion disks – stars: distances – white dwarfs

1. Introduction

AM CVn stars occupy the extreme short period tail of stellar binaries, with observed orbital periods in the range ~5–65 min. They consist of white dwarfs accreting material from Roche lobe-filling companion stars, typically a lower mass white dwarf or a semi-degenerate helium-rich star. The mass transfer in these binaries is driven by gravitational wave radiation and they are expected to be strong sources of low frequency gravitational waves (Nelemans et al. 2004). In particular, the fact that their binary properties such as orbital period and mass ratio can be measured from electromagnetic observations makes them useful as "verification sources" for the Laser Interferometer Space Antenna (LISA) mission. In a separate paper, we predict the gravitational wave strain of the 16 currently-known LISA verification binaries, 11 of which are AM CVn stars (Kupfer et al. 2018).

There are three proposed channels for the formation of AM CVn stars, but their relative importance is not yet clear. The population synthesis models of Nelemans et al. (2001a) suggest that the majority of AM CVn stars form from double white dwarf binaries that evolve closer together as a result of gravitational wave radiation, and start mass transfer at orbital periods of ~2–3 min (Paczyński 1967). Given these small orbital separations, the initial mass transfer occurs as direct impact, which will lead to unstable mass transfer and hence merger in the majority of cases. The fraction of double white dwarfs which survive to become stable mass transferring AM CVn stars is highly uncertain, and depends on the efficiency with which the spin of the accretor can be tidally coupled to the binary orbit to stabilise the mass transfer (Marsh et al. 2004). There has also been a suggestion by Shen (2015) that due to increased friction from ejected material in nova eruptions earlier in the evolution of the binary, all double white dwarf binaries will merge, and that no AM CVn stars should form in this way.

The alternative is that the companion is a core helium-burning star instead of another white dwarf (Savonije et al. 1986; Iben & Tutukov 1987). Such a binary will reach a minimum period of ~10 min before mass transfer starts and the helium star will get increasingly degenerate as it evolves to longer periods.

* Photometry of AM CVn stars is also available at the CDS via anonymous ftp to cdsarc.u-strasbg.fr (130.79.128.5) or via http://cdsarc.u-strasbg.fr/viz-bin/qcat?J/A+A/620/A141

A third channel involves a hydrogen-rich cataclysmic variable with a donor that is already partially evolved at the onset of mass transfer. The binary then loses its hydrogen through evolution and accretion to become an AM CVn star with a period at the long end of the range. It is considered an unimportant channel compared to the white dwarf and helium star scenarios given the long evolutionary timescales involved, but potential progenitor binaries for this channel have been identified (Breedt et al. 2012; Carter et al. 2013b).

Only the two eclipsing AM CVn stars, YZ LMi (SDSS J0926+3624) and Gaia14aae, have parameters measured to high enough precision to discriminate between these models. YZ LMi is likely to be of helium star origin, although the white dwarf route cannot be ruled out completely (Copperwheat et al. 2011). Gaia14aae on the other hand, is inconsistent with a white dwarf donor scenario, but it is also not straightforwardly compatible with either of the other models (Green et al. 2018b). A detailed discussion of the three formation channels and a review of the observed properties of the AM CVn population is given by Solheim (2010).

A well-defined sample of AM CVn stars from the Sloan Digital Sky Survey (SDSS) made it possible to compare the observed space density of these binaries, $\rho = (5 \pm 3) \times 10^{-7}$ pc^{-3}, to population synthesis predictions (Carter et al. 2013a). Even though the models take into account a range of efficiencies for the spin-orbit coupling and the subsequent AM CVn survival rate, the models overpredict the space density by an order of magnitude. The reason for the discrepancy is not clear, but may be related to the uncertainty of the distribution of these binaries in the Galaxy (Nissanke et al. 2012). Most surveys where AM CVn stars have been found have covered only high Galactic latitudes, and it is possible that a substantial fraction reside in the Galactic plane.

One of the main limitations in modelling the spatial distribution of the AM CVn population and calibrating models of space density and luminosity is the lack of accurate distances. Only five systems have a parallax determined using the *Hubble* Space Telescope Fine Guidance Sensor (HST FGS; Roelofs et al. 2007b) with distances to others are generally estimated by comparing model fluxes with observations. With reliable distances we can determine the mass transfer rate, $\dot{M}$, which in conjunction with an orbital period, can constrain which of the three formation channels the binary formed. In turn, this can provide a more reliable value for their space density.

The *Gaia* Data Release 2 (DR2) on 25 April 2018 provided the parallaxes of 1.3 billion stars down to $G \sim 21$ (Gaia Collaboration 2018a) and has allowed us to determine the distances to 41 of the 56 known AM CVn stars. The first *Gaia* data release (DR1; Gaia Collaboration 2016b) in September 2016 relied on a combined *Tycho-Gaia* astrometric solution (TGAS; Gaia Collaboration 2016a), and did not include any AM CVn stars. However, it included parallaxes of 16 hydrogen cataclysmic variables (CVs; Ramsay et al. 2017), which provided a validation of the Disc Instability Model which is widely used to model accreting binaries, including AM CVn stars (Osaki 1989; Kotko et al. 2012; Cannizzo & Nelemans 2015). Another key result from this work was the comparison between the HST FGS, Very Large Array radio data and *Gaia* DR1 parallax measurements of the CV SS Cyg, which resolved a long-standing discrepancy in the distance to (and hence luminosity of) this system, and showed that the HST parallaxes may be unreliable.

In this paper, we use the GDR2 parallax measurements to determine the absolute magnitudes of AM CVn stars and their mass accretion rates. We then use these results to infer the space density of these binaries.

2. The known AM CVn stars

Observationally, AM CVn stars are characterised by their hydrogen deficient optical spectra and blue colour, so surveys for AM CVn stars have typically focussed on these properties to identify new members of the class. The past decade has seen a rapid increase in the number of known AM CVn stars. Firstly because of a dedicated spectroscopic survey of colour-selected targets from SDSS (Carter et al. 2013a, and references therein) and secondly from photometric and spectroscopic follow-up of transient events in large area photometric surveys, such as the Catalina Real-time Transient Survey (CRTS; Breedt et al. 2014), the Palomar Transient Factory (PTF; Levitan et al. 2015) and the All-Sky Automated Survey for Supernovae (ASASSN; Breedt 2015).

Since the data compilation by Levitan et al. (2015), a number of additional AM CVn systems have been discovered. Some of the more recent discoveries include Gaia14aae, the first in which the white dwarf is fully eclipsed (Campbell et al. 2015; Green et al. 2018b), ASASSN-15fp, the longest period AM CVn system to have been observed in outburst so far (Cartier et al. 2017; Marsh et al. 2017), and SDSS J1351-0643, the first system with a period shorter than 17 min to be discovered in ~15 years (Green et al. 2018c). In Table 1, we list the 56 AM CVn stars known at present, ordered by increasing orbital period. We provide a full table, including J2000.0 and J2015.5 sky coordinates and multi-wavelength photometry at the CDS. The column description of the full table is shown in Appendix A.

Time series spectroscopy remains the most reliable method to measure the orbital periods of AM CVn stars, but it is a challenging task due to the faintness of many systems and the short exposures which are needed to phase resolve the short orbital period. For systems which display outbursts (see Table 1) the superhump period may be used as a proxy. These are flux variations observed during superoutbursts, resulting from the interaction between the precessing accretion disc and the donor star (e.g. Wood et al. 2011). It is typically a few per cent longer than the orbital period. Other proxies include the relationship between the equivalent width of emission lines and the orbital period (Carter et al. 2013a), and the recurrence time between outbursts (Levitan et al. 2015).

The orbital periods of the known AM CVn stars range from 5.4 min to 65.6 min. Eight of the known systems do not have an estimate of their orbital period yet. AM CVn stars at the short period end ($P_{\rm orb} < 20$ min), are akin to novalike CVs, with hot, high state accretion discs. The accretion rate drops as the binary evolves to longer periods, and at the longest periods in the range (i.e. lowest accretion rates) the discs are in a low, stable state. At intermediate periods, $20 < P_{\rm orb} \lesssim 44-52$ min, the discs display ~1–5 mag outbursts similar to the dwarf nova outbursts observed in the hydrogen cataclysmic variables (Levitan et al. 2011, 2015; Ramsay et al. 2012). The long period boundary below which outbursts are observed is not sharp. For example, Gaia14aae and ASASSN-15fp, with periods of 49.7 and 51.0 min respectively, were discovered as a result of their outbursts, but the long-known system GP Com with $P_{\rm orb} = 46.6$ min, has never been observed in outburst. Cannizzo & Nelemans (2015) show that this is a result of the dependence of the mass transfer rate on the accretor mass, in the sense that systems with a more massive accretor have a higher mass transfer rate at a given orbital period. This dependence is stronger at the long period edge than at the short period edge, resulting in a mix of outbursting and stable systems near $P_{\rm orb} \sim 44-52$ min.

Table 1. Currently known AM CVn stars ordered by increasing period, either the orbital period (most reliably determined from spectroscopic observations) or the superhump period (sh) which is typically within a few percent longer than the orbital period.

Source	Period (mins)	Outbursts?	Mag. Range (filter)	Reference	Parallax (mas)	σ (mas)	Distance (pc)	σ (pc)
HM Cnc	5.4	✗	21.1	1	0.095	0.327	1786	667
V407 Vul	9.5	✗	19.9 (V)	2	0.596	0.108	1584	291
ES Cet	10.4	✗	16.5–16.8	3	0.596	0.313	1317	531
SDSS J1351-0643	15.7	✗	18.6	43	3.351	0.045	299.1	4.4
AM CVn	17.1	✗	14.2	4	0.954	0.046	1044	51
SDSS J1908+3940	18.1	✗	16.1	5, 6	3.62	0.05	276	4
HP Lib	18.4	✗	13.6–13.7	7	0.550	0.327	1339	555
PTF1 J1919+4815	22.5	✓	18.2–21.8	8	1.016	0.146	971	156
CX361	22.9	✗	17.6	9	0.975	0.098	1019	108
ASASSN-14cc	22.5 (sh)	✓	16.0–20.0 (V)	10				
CR Boo	24.5	✓	13.8–17.0	11	1.035	0.149	956	153
KL Dra	25.0	✓	16.0–19.6	12				
PTF1 J2219+3135	26.1 (p)	✓	16.2–20.6	14				
V803 Cen	26.6	✓	12.8–17.0	13, 14	1.144	0.301	861	304
PTF1 J0719+4858	26.8	✓	15.8–19.4	15				
ASASSN-15kf	27.7 (sh)	✓	15.0 (V) –19.4 (B)	16, 17	1.824	0.549	577	324
YZ LMi (SDSS J0926+3624)	28.3	✓	16.6–19.6	18	0.684	0.941	964	615
CP Eri	28.4	✓	16.2–20.2	19	0.830	0.668	979	575
SDSS J1043+5632	28.5:(p)	✓	17.0–20.3	14	0.695	0.477	1113	561
CRTS J0910-2008	29.7 (sh)	✓	14.0–20.4 (g)	45				
PTF1 J0943+1029	30.4	✓	16.9 (R)–20.7 (g)	20	1.382	0.457	734	374
CRTS J0105+1903	31.6	✓	16.3-19.6	21, 22				
PTF1 J1632+3511	32.7 (p)	✓	17.9–23.0	20				
CRTS J0744+3254	33: (p)	✓	17.4–21.1	14	2.391	1.050	504	493
V406 Hya	33.8	✓	14.5–19.7	23				
PTF1J0435+0029	34.3	✓	18.4 (R) – 22.3 (g)	20	1.061	0.382	911	420
SDSS J1730+5545	35.2	~	18.5 (V) –20.1	14, 24a	1.911	1.425	677	595
V558 Vir (2QZ J1427-0123)	36.6 (sh)	✓	15.0–20.5	25	1.857	0.611	577	365
SDSS J1240-0159	37.4	✓	16.8–19.8	27	2.971	0.142	337	17
NSV1440	37.5 (sh)	✓	12.4(V) – 17.9(G)	45	2.066	0.529	508	239
V744 And (SDSS J0129+3842)	37.6	✓	14.5–19.8	14, 26, 29	0.798	0.665	995	578
SDSS J1721+2733	38.1	✓	16.0–20.1	14, 31	4.069	0.119	247	7
ASASSN-14mv	41: (sh)	✓	11.8 (V) – 18.1 (V)	16, 17, 44	3.92	0.045	255	4
ASASSN-14ei	43: (sh)	✓	11.9–17.6 (B)	17, 33	1.928	0.276	524	9(
SDSS J1525+3600	44.3	✗	20.2	31	1.203	0.210	828	17
SDSS J0804+1616	44.5	✓	17.8–19.0	28, 30	2.361	0.305	429	6
SDSS J1411+4812	46.0	✓	12.4–19.7	29, 30, 48	13.731	0.060	73.0	0.
GP Com	46.6	✗	15.9–16.3	32				
CRTS J0450-0931	47.3 (sh)	✓	14.8–20.5	34	2.519	0.936	461	4
SDSS J0902+3819	48.3	✓	13.8 (V) – 20.2 (g)	15, 31, 35	3.871	0.155	259	
Gaia14aae	49.7	✓	13.6 (V) – 18.7 (g)	36, 49				
ASASSN-17fp	51.0 (sh)	✓	15.7–20+	37	5.005	0.416	202	
SDSS J1208+3550	53.0	✗	18.9–19.4	30, 38, 39	0.621	0.730	1044	6
SDSS J1642+1934	54.2	✗	20.3	31, 39	2.395	0.609	443	
SDSS J1552+3201	56.3	✗	20.2–20.6	30, 41	4.838	0.310	209	
SDSS J1137+4054	59.6:	✗	19.0	24b	10.694	0.148	93.6	
V396 Hya	65.1	✗	17.6	42	4.894	0.240	205	
SDSS J1319+5915	65.6	✗	19.1	40,47				
PU Aqr (SDSS J2047+0008)	?	✓	17.0–24	38	0.395	0.341	1474	
CRTS J0844-0128	?	✓	17.4–20.3	14				
PTF1 J0857+0729	?	✓	18.6–21.8	14	6.299	0.453	160	
SDSS J1505+0659	?	✗	19.1	24b				
PTF1 J1523+1845	?	✓	17.6–23.5	14				
ASASSN-14fv	?	✓	14.6 (V) – 20.5 (B)	41	0.760	0.859	956	
Gaia16all	?	✓	16.2 – 20.6(G)	46	0.055	2.42	883	
SDSS J0807+4852	?	✗	19.5(V)–20.4(g)	50				

Notes. (p) implies the predicted orbital period based on the outburst properties (Levitan et al. 2015). ✓ or ✗ indicates whether the source h
seen in outburst. The references and full coordinates are given in Appendix A.2.

Table 2. *Gaia* DR2 and HST parallaxes of the five AM CVn stars which were measured using the HST Fine Guidance Sensor.

Source	HST parallax (mas)	*Gaia* parallax (mas)
AM CVn	1.65 ± 0.30	3.351 ± 0.045
HP Lib	5.07 ± 0.33	3.622 ± 0.053
CR Boo	2.97 ± 0.34	N/A
V803 Cen	2.88 ± 0.24	N/A
GP Com	13.34 ± 0.33	13.73 ± 0.06

3. Parallaxes and distances of AM CVns in *Gaia* DR2

In Table 1 we show the parallaxes for all AM CVn stars included in the *Gaia* DR2: out of the 56 known systems 41 have parallax measurements. The closest system is the long known GP Com with a parallax of 13.73 ± 0.06 mas, with the most distant being V407 Vul which has a parallax consistent with zero (0.10 ± 0.33 mas). In Table 2 we compare the parallaxes for three sources which have both *Gaia* and HST parallaxes (V803 Cen and CR Boo have no parallax in *Gaia* DR2). There is reasonable agreement for GP Com. However, HP Lib is significantly more distant and AM CVn significantly closer compared to the results of HST. Indeed the HST parallax derived for AM CVn implied a greater distance than other estimates and therefore implied a high luminosity and mass accretion rate, all of which were problematic in explaining.

We convert parallaxes from the *Gaia* DR2 into distances following the guidelines from Bailer-Jones (2015), Astraatmadja & Bailer-Jones (2016) and Gaia Collaboration (2018c). Given the measured parallax ϖ with the uncertainty σ_ϖ, the probability density of possible values for the distance can be found by using Bayes' theorem:

$$P(r|\varpi, \sigma_\varpi) = \frac{1}{Z} P(\varpi|r, \sigma_\varpi)\, P(r), \quad (1)$$

where r is the distance, $P(\varpi|r, \sigma_\varpi)$ is the likelihood function, that can be assumed Gaussian (Gaia Collaboration 2018b). $P(r)$ is the prior and Z is a normalisation constant. The prior is an arbitrary function that expresses our knowledge on the distribution of the distances of AM CVn stars and allows us to introduce assumptions in the inference procedure that are not related to the measurement of the parallax itself. The properties of various priors and their performance on the data from the *Gaia* DR1 have been investigated in Astraatmadja & Bailer-Jones (2016). For this work we adopt the exponentially decreasing space density prior:

$$P(r) = \begin{cases} \frac{r^2}{2L^3} \exp(-r/L) & \text{if } r > 0, \\ 0 & \text{otherwise,} \end{cases} \quad (2)$$

where L is the scale length. This prior implies a constant space density of AM CVn stars for $r \ll L$ and an exponential drop for $r \gg 2L$, where $2L$ corresponds to the peak of the distribution. The choice of the value for L needs to be fine-tuned to reproduce the distribution of AM CVn stars with the distance. We adopt $L = 400$ pc calibrated on the mock population of double white dwarf binaries (progenitor systems of AM CVns) from Korol et al. (2017). For more detailed argumentation we refer the reader to Kupfer et al. (2018). In Table 1 we show the inferred distance and uncertainty (which covers the 90 percent confidence interval) for those AM CVn systems which have parallax measurements in the *Gaia* DR2. The distances range from 73 pc (GP Com) to 1.8 kpc (V407 Vul), although the latter is rather uncertain. The median distance is 580 pc. For sources closer than 340 pc the mean uncertainty on the distance is 9 pc, and for those between 500–1000 pc it is 380 pc.

4. Galactic distribution

For the 41 systems with parallax and proper motions from *Gaia* DR2 (shown in Table B.1), we calculate 3D kinematics and put constraints on their population membership: thin disc, thick disc, and halo. Only AM CVn, SDSSJ 1908+3940, CP Eri, SDSS J1730+5545 and SDSS J1240-0159 have measured systemic velocities based on radial velocity curves of their accretion disc lines. Seven additional systems have a strong central spike feature which can be used to measure the radial velocity. These central spike lines are believed to originate close to the photosphere of the accretor and are shifted with the gravitational redshift of the accretor. Assuming an accretor with $M = 0.8\,M_\odot$ and a radius of $R = 0.01\,R_\odot$ leads to a gravitational redshift of 50 km s^{-1}, so we correct the measured velocity from the central spike by 50 km s^{-1}. For the remaining systems with no measured radial velocity, we assume 0 km s^{-1} with an error of ± 50 km s^{-1}.

Combined with right ascension and declination, we calculate velocity in the direction of the Galactic Centre (V_ρ) and the Galactic rotation direction (V_ϕ), the Galactic orbital eccentricity (e), and the angular momentum in the Galactic z direction (J_z). The Galactic radial velocity V_ρ is negative towards the Galactic centre, while stars that are revolving on retrograde orbits around the Galactic Centre have negative V_ϕ. Stars on retrograde orbits have positive J_z. Thin disc stars generally have very low eccentricities e. Population membership can be derived from the position in the $V_\rho - V_\phi$ diagram and the $J_z - e$ diagram following the description in Pauli et al. (2003, 2006).

We show the results in Fig. 1. We find that the most of the systems show a Galactic orbit typical for a thin disc population (see Table B.1). About 10 systems have a typical thick disc orbit. None of the systems show a halo orbit. In a small number of AM CVn stars, the extreme depletion of heavy elements have been taken as evidence that these stars were halo objects (GP Com: Marsh et al. 1991; V396 Hya: Nagel et al. 2009 and PTF1 J0719+4858: Gehron et al. 2014). Our study has shown that these AM CVn stars are likely thin or thick disc objects and not halo objects. It is of interest to understand how disc objects can have such low abundances of heavy elements.

5. Determining the line of sight extinction

To determine the absolute magnitude of AM CVn stars we need to subtract the effects of interstellar extinction. Although 47 of the 56 AM CVn stars shown in Table 1 lie at Galactic latitudes $|b| > 20°$ (implying the extinction is likely to be low), we have determined the line-of-sight extinction to our sources using 3D-dust maps derived from Pan-STARRS1 data (Green et al. 2018a). For each AM CVn star, we derived the extinction, E_{B-V}, for the sky co-ordinates and distance of that star given in Table 1 (the uncertainty is typically $E_{B-V} \sim 0.02$). To determine the reddening, we use $A_V = R \times E_{B-V}$, where we assume the standard value of $R = 3.2$. To obtain the reddening in the g band, we assume $Ag = 1.1 \times A_V$ (Cardelli et al. 1989). For those AM CVn stars at declinations too south to feature in the Pan-STARRS1 catalogue we use the dustmaps of Schlafly & Finkbeiner (2011)

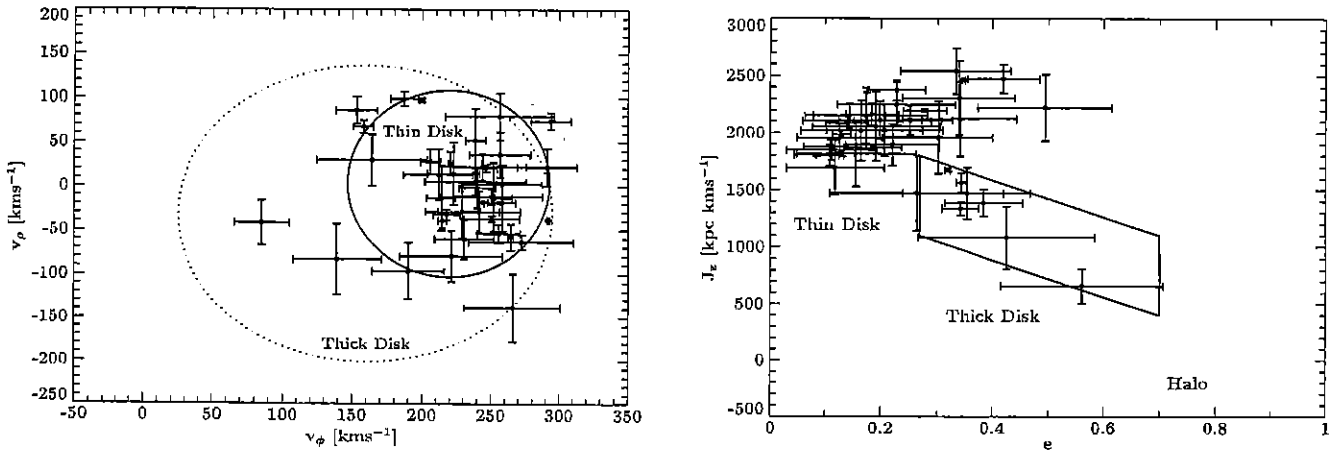

Fig. 1. AM CVn stars in the plane of the velocity in the direction of Galactic rotation (V_ϕ) and the Galactic centre (V_ρ) (*left hand panel*) and the orbital eccentricity (e) and the angular momentum in the Galactic z direction(J_z) (*right hand panel*). The solid and dotted ellipses render the 3σ thin and thick disc contours in the V_ϕ–V_ρ diagram, while the solid box in the e–J_z marks the thick disc region as specified by Pauli et al. (2006).

which give the extinction to the edge of the Galaxy in that line of sight (this step was required for only two stars and given that the upper limits are only 0.2 mag, we do not expect that this uncertainty will significantly effect their place on the period – absolute magnitude relationship).

We show the reddening to those AM CVn stars with parallaxes in Table 3. The median reddening of our sample is $A_g = 0.14$ mag, with 90 percent of sources having $A_g < 0.35$ mag. Therefore for the majority of our targets the effects of interstellar absorption has a small effect on the resulting absolute magnitudes. The only source with a high extinction, V407 Vul, was previously known to have a high degree of reddening (Motch et al. 1996).

6. The absolute magnitudes of AM CVn stars

Using the distances shown in Table 1, we show in Fig. 2 the absolute magnitude, M_G, against the BP-RP (the "Blue Photometer" and "Red Photometer" colour derived from *Gaia* data) of AM CVn stars and a sample of Galactic stars with accurate parallax measurements. The single white dwarf track can be seen in the lower left of the figure. High state AM CVn stars are significantly brighter than the isolated white dwarfs, being $M_G \sim 6$. The majority of quiescent AM CVn stars appear 1–2 mag brighter than the white dwarfs, being $M_G \sim 8$–12, though a minority lie on the white dwarf track.

As the wavelength range of the *Gaia* G band filter is very broad, it is not the optimal filter with which to test evolutionary models which usually predict the absolute magnitude in the V or g bands. We have therefore collated all the available multi-filter photometry of the AM CVn stars from the Pan-STARSS1, Skymapper, GALEX and SDSS surveys and we show these in Appendices A.4–A.7 and associated tables. Since most surveys release mean or median values for each source and filter, the effects of outbursts are generally smoothed out and usually they reflect the quiescent brightness for outbursting systems. In Table 3 we show the mean quiescent g mag which we derive for these systems. For most systems this magnitude is found from analysis of the g-band data shown in the appendix. In the case of ASASSN-14cc, a short-period system which is in outburst for around 60 percent of the time, the magnitude measured by Skymapper is representative of its outburst magnitude. We therefore take its quiescent magnitude from Kato et al. (2015).

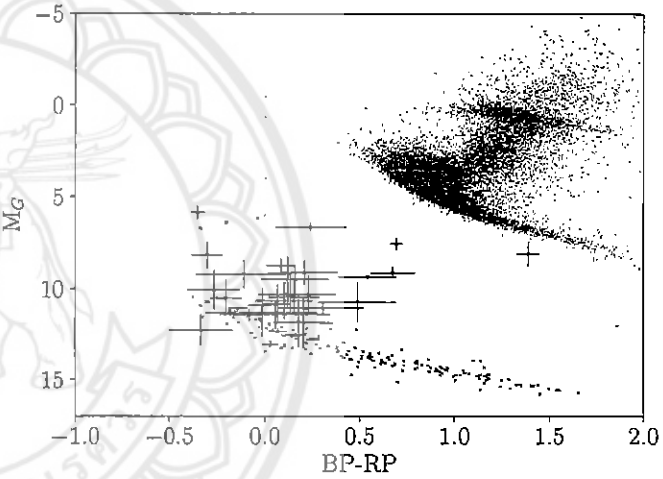

Fig. 2. An HR diagram made using *Gaia* DR2 data. In red we show the absolute G magnitude, M_G, as a function of the blue-red colour, BP-RP, for AM CVns with known parallaxes. No reddening or extinction corrections have been applied to this figure. For comparison, in grey points we show a sample of essentially randomly selected main sequence stars which have a parallax better than 1 percent. For single white dwarfs shown as slightly larger grey points) we have used the sample of white dwarfs within 20 pc (Hollands et al. 2018). The majority of AM CVns appear to be brighter than the single white dwarf track, though some long-period systems lie on the track. A clear outlier is V407 Vul, which has BP-RP ≈ 1.5 through a combination of severe reddening and contamination from an unresolved nearby G-star.

Based on these quiescent magnitudes, we calculate the absolute magnitudes shown in Table 3. In Fig. 3 we plot the absolute magnitudes of AM CVn binaries as a function of orbital period, for the 37 systems in which both magnitude and orbital period are known. For those systems which outburst we also plot an approximate outburst magnitude. For comparison, we show the predicted magnitudes of the central white dwarf and the accretion disc, both of which vary in magnitude as a function of orbital period. We show two cooling tracks for a 0.65 $M_\odot$ central white dwarf, both taken from Bildsten et al. (2006): one assumes a low mass transfer rate (as would be seen for a cool, low-mass white dwarf donor) and one assumes a high mass transfer rate (as would be seen in a hot, high-mass dwarf donor). The donor

Table 3. Reddening in the g band (A_g), which have been determined using Pan-STARRS1 data (Green et al. 2018a).

Source	P_{orb} (min)	A_g (mag)	g_q (mag)	M_g (mag)
V407 Vul	9.5	4.9	20.16	4.0 ± 0.7
ES Cet	10.4	0.1	16.66	5.6 ± 0.4
SDSS J1351-0643	15.7	0.1	18.66	8.0 ± 0.7
AM CVn	17.1	0.07	14.26	6.81 ± 0.03
SDSS J1908+3940	18.1	0.53	16.16	5.5 ± 0.1
HP Lib	18.4	0.49	13.60	5.91 ± 0.03
PTF1 J1919+4815	22.5	0.18	20.51	9.7 ± 0.8
CX361	22.9	1.16	17.48	6.4 ± 0.3
ASASSN-14cc	22.5	0.12	19.0	8.9 ± 0.2
KL Dra	25.0	0.18	18.62	8.5 ± 0.3
PTF1 J0719+4858	26.8	0.32	19.15	9.2 ± 0.7
YZ LMi	28.3	0.07	19.23	10.4 ± 1.0
CP Eri	28.4	0.35	20.07	9.8 ± 1.1
SDSS J1043+5632	28.5	0.07	20.35	10.33 ± 1.0
CRTS J0910-2008	30.2	0.32	19.39	9.9 ± 0.9
CRTS J0105+1903	31.6	0.18	19.65	10.1 ± 0.9
V406 Hya	33.8	0.11	19.97	11.4 ± 1.5
SDSS J1730+5545	35.2	0.14	20.05	10.1 ± 0.8
NSV1440	36.3	0.21^m	18.53	10.7 ± 0.1
V558 Vir	36.6	0.14	19.99	10.7 ± 1.4
SDSS J1240-0159	37.4	0.07	19.55	10.7 ± 1.1
V744 And	37.6	0.28	19.88	11.1 ± 0.8
SDSS J1721+2733	38.1	0.07	20.43	10.4 ± 1.0
ASASSN-14mv	41	0.04	17.98	11.0 ± 0.1
ASASSN-14ei	43	0.21^m	15.54	8.94 ± 0.03
SDSS J1525+3600	44.3	0.07	19.86	11.2 ± 0.3
SDSS J0804+1616	44.5	0.18	18.60	8.8 ± 0.4
SDSS J1411+4812	46.0	0.07	19.44	11.2 ± 0.3
GP Com	46.6	0.00	15.92	11.60 ± 0.01
SDSS J0902+3819	48.3	0.11	20.39	12.0 ± 1.4
Gaia14aae	49.7	0.04	18.55	11.4 ± 0.1
SDSS J1208+3550	53.0	0.07	18.82	12.2 ± 0.2
SDSS J1642+1934	54.2	0.25	20.35	10.0 ± 1.0
SDSS J1552+3201	56.3	0.14	20.40	12.0 ± 0.9
SDSS J1137+4054	59.6	0.07	19.09	12.4 ± 0.1
V396 Hya	65.1	0.18	17.68	12.64 ± 0.03
SDSS J1319+5915	65.6	0.04	19.12	12.6 ± 0.1

Notes. Those stars where the reddening has been estimated using the dust maps of (Schlafly & Finkbeiner 2011) have a superscript m to indicate it is the reddening to the edge of the Galaxy. The third column shows the quiescent g magnitude as determined from the survey magnitudes outlined in the appendix. In the final column we show the absolute magnitude, M_g. These data are also included in the online table.

masses assumed span the range of white dwarf donor masses predicted by Deloye et al. (2005), but we note that higher-mass donors are possible through other evolutionary channels. The accretion disc magnitudes are calculated by Nelemans et al. (2004).

As Fig. 3 shows, a strong decrease in AM CVn absolute magnitude with increasing orbital period is seen. High-state systems ($P_{orb} \lesssim 20$min) lie close to the predicted accretion disc magnitudes, as expected for these disc-dominated systems. Quiescent systems lie a little above the white dwarf cooling track, with an excess that generally decreases with increasing period, though there is considerable scatter between systems. For outbursting

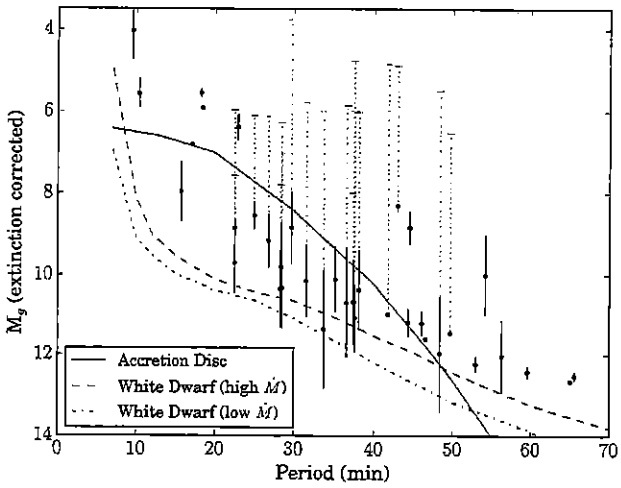

Fig. 3. Extinction-corrected absolute magnitudes (M_g) of AM CVn binaries as a function of orbital period. For known outbursting systems, we plot the quiescent magnitude, and show the magnitude change during outburst as a dotted line. The dashed line is the predicted M_V of the accretion disc as originally taken from Nelemans et al. (2004) while the solid line shows the evolution of a $0.65M_\odot$ accreting white dwarf with a high-entropy white dwarf donor, including accretion heating, from Bildsten et al. (2006). Most systems appear somewhat brighter than an isolated white dwarf model during quiescence, and close to the duty-cycle-scaled disc magnitude during outburst.

systems, the outburst magnitude in most cases is far in excess of the mean disc magnitude.

All AM CVn systems shown in Fig. 3 are brighter than the predicted white dwarf cooling track for a high-mass white dwarf donor, and significantly brighter than the cooling track for a low-mass white dwarf donor. For systems at $P_{orb} > 50$ min, which are dominated by their white dwarf magnitudes, this is particularly interesting. It may suggest that AM CVn donors have a systematically higher mass than predicted. Measurements of AM CVn mass ratios imply a similar trend (Green et al. 2018c). If true, this would imply either that white dwarf donors have higher temperatures (and hence higher masses for a given orbital period) than predicted, or that the majority of systems have non-white dwarf donors.

Several individual systems are worthy of note:

- V407 Vul appears unusually bright due to the G star which is co-aligned on the sky. Barros et al. (2007) estimated that the G star contributes 92% of the light in the g-band, giving a magnitude difference of 2.7.
- SDSS J1351-0643 has an unexpectedly low magnitude for a high-state system, though its uncertainties are large. This low magnitude could be explained if the system is at a high inclination, such that the disc is viewed close to edge-on. Its broad double-peaked spectrum and photometrically-visible disc precession also support a high inclination.
- ASASSN-14ei, SDSS J0804+1616, Gaia14aae, and SDSS J1642+1934 seem to be unusually bright for their orbital period. For some of these systems there is evidence they may have a high mass transfer rate: SDSS J0804+1616 is unusually variable (Ramsay et al. 2012), while Gaia14aae is among the longest-period outbursting AM CVns and has an unexpectedly high-mass donor star (Campbell et al. 2015; Green et al. 2018b). As discussed in Sect. 7, the elevated magnitude of Gaia14aae is almost entirely due to its hot central white dwarf.

– Several systems have outburst magnitudes that are lower than the general trend, including PTF1 J1919+4815, YZ LMi, and SDSS J1240-0159. The first two of these systems are partial eclipsers and therefore high-inclination, which will reduce the observed outburst magnitude. The reason for the weak outburst of SDSS J1240-0159, reported by Roelofs (2007), is uncertain.

7. Component magnitudes of eclipsing AM CVns

Three AM CVns are currently known which undergo eclipses. In Gaia14aae and YZ LMi, the central white dwarf is eclipsed, while in PTFJ 1919+4815, only the edge of the disc is eclipsed. The first two systems present an opportunity to measure the flux contributions from, and hence absolute magnitudes of, their central white dwarfs. We can additionally measure the flux contribution from the 'bright spot' component of these systems, this being a bright region located at the point of collision between the accretion disc and the stream of infalling matter from the donor.

Photometry of YZ LMi in Sloan *ugr* bands and of Gaia14aae in *ugri* bands were presented in Copperwheat et al. (2011) and Green et al. (2018b) respectively. Both papers quote the measured white dwarf fluxes, from which we calculate the absolute magnitudes. To calculate the bright spot contributions, we obtained the best-fit models presented in both papers and measured the bright spot contribution directly. Uncertainties were calculated from the 1-σ spread of the MCMC results created for those papers when converging on the data. The absolute magnitudes we calculate for these components are presented in Table 4. In the case of YZ LMi, large uncertainties result from the poorly constrained *Gaia* parallax of the system. The *i*-band Gaia14aae magnitudes are poorly constrained due to the small number of eclipses observed in that band.

7.1. Central white dwarfs

These central white dwarf magnitudes may be compared with the predicted white dwarf magnitude track shown in Fig. 3, for corresponding orbital periods. It should be noted that both white dwarfs are somewhat higher mass ($\approx 0.85\,M_\odot$) than the mass assumed in that model ($0.65\,M_\odot$). A larger mass effects the magnitude in two ways: the reduction in size of the white dwarf causes it to appear fainter, but the smaller surface area increases the effect of accretion heating on temperature. With this caveat, the central white dwarf *g* magnitude of YZ LMi agrees reasonably well with the predicted value of 10.6. For Gaia14aae, the central white dwarf magnitude of 11.66(9) is considerably brighter than the predicted magnitude of 12.4. As shown in Bildsten et al. (2006), the white dwarf mass is less significant than accretion rate for long-period systems like Gaia14aae. It therefore seems likely that the elevation of the central white dwarf magnitude of Gaia14aae above the model track is due to a higher accretion rate than predicted, resulting in a hotter white dwarf.

Given the tightly constrained absolute magnitudes of Gaia14aae, the temperature of the central white dwarf can be estimated. From DB atmosphere models (Bergeron et al. 2011; Tremblay et al. 2011; Kowalski & Saumon 2006; Holberg & Bergeron 2006), for a surface gravity $\log(g) \approx 8.5$ as measured by Green et al. (2018b), these magnitudes in all four colour bands predict a temperature of $\approx 17\,000 \pm 1000$ K. This temperature disagrees with the previously established temperature of $12\,900 \pm 200$ K established from UV flux (Campbell et al. 2015). The discrepancy may be the result of metals accreted from the donor star, in particular nitrogen, which are expected given the evolved nature of the donor (Nelemans et al. 2010). Such metals would cause absorption in the UV not present in a pure DB atmosphere, making the UV-derived temperature unreliable. We therefore interpret 17 000 K as the most likely temperature of the white dwarf.

Table 4. Absolute magnitudes of the central white dwarfs and bright spots in two eclipsing systems: YZ LMi and Gaia14aae.

Source	Filter	White Dwarf	Bright Spot
YZ LMi	*r*	10.9(1.0)	14.7(1.6)
	g	11.2(1.0)	14.1(1.5)
	u	10.7(1.0)	14.5(1.6)
Gaia14aae	*i*	12.17(10)	15.7(1.1)
	r	11.95(9)	14.6(2)
	g	11.66(9)	14.8(2)
	u	11.58(10)	14.4(7)

7.2. Bright spots

The magnitudes of the bright spots in these systems allow for their instantaneous mass transfer rates, $\dot{M}$, to be estimated. If the luminosity of the bright spot is equal to the kinetic energy released by the infalling matter as it slows to match the disc velocity, the luminosity can be described as

$$L = \frac{1}{2}\dot{M}|V_{\rm stream} - V_{\rm disc}|^2 \quad (3)$$

where $V_{\rm stream}$ and $V_{\rm disc}$ are vectors describing the velocities of material in the stream and disc at the point of intersection between the two. Assuming that the disc material follows a Keplerian orbit and that the stream trajectory is ballistic, these can be calculated based on the measured stellar masses of the system. The luminosity found by Eq. (3) can then be converted to a magnitude using an assumed spectral response for the bright spot. We assume the spectral response of a 12000 K black-body, as was observed for the cataclysmic variable IP Peg (Marsh 1988). To account for our uncertainty in this choice of spectral response, we increase the uncertainties on the predicted magnitude by 0.2 mag, and propagate this through to the uncertainties on $\dot{M}$. We find $\log(\dot{M}/M_\odot\,{\rm yr}^{-1}) = -10.6 \pm 0.4$ for YZ LMi and -10.74 ± 0.07 for Gaia14aae.

For comparison we calculate theoretical values of $\dot{M}$ based on the photometrically measured masses, using the relations in Deloye et al. (2007). It is necessary to assume a value for the donor star's response to mass loss, $\mathrm{d}\log(R)/\mathrm{d}\log(M)$. For this we assume 0.2, which approximates the tracks in Deloye et al. (2007) for donors evolving isothermally. For YZ LMi, the predicted $\log(\dot{M}/M_\odot\,{\rm yr}^{-1}) = 10.0$ is within 1.5-σ of our measured value. Given that these uncertainties are likely to be non-Gaussian, we do not consider this discrepancy to be significant. In the case of Gaia14aae, an assumed donor response of 0.2 implies $\log(\dot{M}/M_\odot{\rm yr}^{-1}) = 10.77$, in good agreement with our measured mass transfer rate.

The agreement in the case of Gaia14aae is, to some extent, surprising. Deloye et al. (2007) predict $\mathrm{d}\log(R)/\mathrm{d}\log(M) = 0.2$ for AM CVn donors during their short-period evolution. However, once they evolve to periods $\gtrsim$40 min, a change of state in the donor is expected that would result in this value decreasing.

Table 5. Mass transfer rates determined by fitting the SED of each system using a model consisting of a white dwarf plus steady-state accretion disc model.

Source	Period (mins)	log10 ($\dot{M}$ ($M_\odot$ yr^{-1})	±	$\dot{M}$ ($M_\odot$ yr^{-1})	±
ES Cet	10.4	−7.61	0.46	2.5×10^{-8}	1.6×10^{-8}
SDSSJ1351	15.7	−8.58	1.13	2.6×10^{-9}	2.4×10^{-9}
SDSSJ1908	18.1	−6.18	0.27	6.6×10^{-7}	3.1×10^{-7}
HP Lib	18.4	−8.26	0.19	5.5×10^{-9}	1.9×10^{-9}
ASASSN-14cc	22.5	−8.63	0.14	2.3×10^{-9}	6.5×10^{-10}
ASASSN-14mv	41.0	−8.59	0.16	2.6×10^{-9}	7.9×10^{-10}
ASASSN-14ei	43.0	−10.14	0.13	7.2×10^{-11}	1.9×10^{-11}
SDSSJ1525	44.3	−10.15	0.46	7.1×10^{-11}	4.6×10^{-11}
SDSSJ1411	46.0	−10.44	0.17	3.6×10^{-11}	1.2×10^{-11}
GP Com	46.6	−10.64	0.25	2.3×10^{-11}	1.0×10^{-11}
Gaia14aae	49.7	−10.48	0.06	3.3×10^{-11}	4.3×10^{-12}
SDSSJ1208	53.0	−11.15	0.15	7.1×10^{-12}	2.1×10^{-12}
SDSSJ1137	59.6	−11.09	0.28	8.1×10^{-12}	3.9×10^{-12}
V396 Hya	65.1	−10.86	0.26	1.4×10^{-11}	6.2×10^{-12}
SDSSJ1319	65.6	−10.94	0.26	1.1×10^{-11}	5.2×10^{-12}

Notes. Apart from the eclipsing system (Gaia14aae), we fixed the mass of the white dwarf at $M_1 = 0.8 \pm 0.1\,M_\odot$ and cos(i) = 0.5. We varied radius of the accretion disc to achieve a good fit. The large error the mass transfer rate of SDSS J1505 is due to the large error on the distance.

The fact that 0.2 still appears to hold for Gaia14aae agrees with our suggestion in Green et al. (2018b) that the donor has not yet undergone this change of state.

Recent work by Piersanti et al. (2015) predict the mass accretion rate for systems with periods shorter than 22 min. However, we use the work of Bildsten et al. (2006) who give a relation between the mass transfer rate and the temperature of the accretion-heated central white dwarf in AM CVn systems for the entire orbital period seen in AM CVn stars. Bildsten et al. (2006) predict that, for long-period ($P \gtrsim 30$ min) and hence low-$\dot{M}$ systems, energy radiated from the white dwarf core will heat the surface more than energy from accretion. The surface temperature will then be higher than would be predicted from $\dot{M}$ alone. This can be seen in Gaia14aae, where the $\dot{M}$ measured above would suggest a black-body white dwarf temperature of 5500 K. The difference between this and our measured temperature of 17 000 K implies, as predicted, that the temperature has decoupled from $\dot{M}$.

8. Mass transfer rate as a function of orbital period

One of the reasons that determining the theoretical space density of AM CVn stars has so many uncertainties, is that although there are three likely formation channels, the relative importance of each channel is not well determined. The formation channels largely differ in the nature of the mass donating star. A white dwarf donor would start mass transfer at short orbital periods, whilst the helium star, or highly evolved CV donor, would initially evolve to short orbital periods before evolving to long periods as the mass donating star becomes fully degenerate (see Solheim 2010 for a detailed overview).

If we were able to accurately determine the mass transfer rate for many sources with a range of orbital period we would make progress in understanding the relative importance of the formation channels since they follow different tracks on the $P_{\rm orb} - \dot{M}$ plane. Determining reliable values for $\dot{M}$ requires photometric information across a wide range of the spectrum, including the UV, where much of the accretion luminosity is emitted (especially for short period systems, for instance, Ramsay et al. 2005, 2006).

For AM CVn stars which have a parallax accurate to within 20 percent, we converted the multi-band photometric data outlined in the appendix to flux units (Jy) (we also included SDSS J1351 since it has a short orbital period – 15.7 min – and is therefore interesting from an evolutionary point of view). Some systems, such as KL Dra and AM CVn show a large scatter between the multi-filter flux measurements (possibly due to outbursts in the case of KL Dra, and perhaps significant flickering in the case of AM CVn) and were therefore not suited to determining their mass transfer rate by this means. There were 15 systems which had suitable data and we show their spectral energy distributions in Fig. B.1. For the shortest orbital period systems, the energy distribution is generally still increasing at our bluest flux point (GALEX FUV). For long period systems we can locate the wavelength which the flux appears to peak.

To determine the mass transfer rate we sum up the contribution of flux emitted from the white dwarf and accretion disc. Although the cooling models of Bildsten et al. (2006) assume that the primary star has a mass of 0.65 $M_\odot$, the primary in both of the eclipsing systems is M_1=0.8 $M_\odot$. We therefore set $M_1 = 0.8 \pm 0.1\,M_\odot$ for the non-eclipsing systems. We calculate the radius of the primary using the formula of Eggleton's quoted in Verbunt & Rappaport (1988). We also assume that the disc is accreting at a steady state and has a number of annuli (40) which we compute the temperature assuming a black-body. Again apart from Gaia14aae the system inclination is not well determined and therefore we fix cos(i) = 0.5 (apart from Gaia14aae where $i = 86.3°$). An additional parameter was the radius of the accretion disc, $r_{\rm out}$. There will be some trade-off between $r_{\rm out}$ and cos(i) which we did not explore in detail.

We use modules readily available in python modules including `astropy`. To determine the mass transfer rate and its uncertainty we randomly select values for distance, mass and extinction within the assigned errors with the other parameters

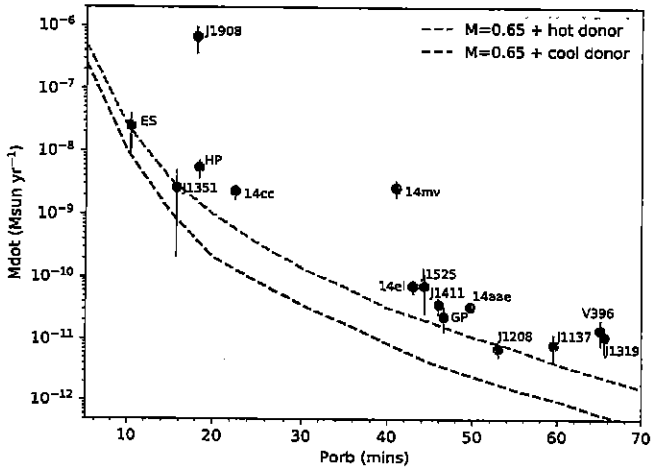

Fig. 4. Predicted mass accretion rate, $\dot{M}$, of Bildsten et al. (2006) as a function of orbital period, where the accretor is a 0.65 $M_{\odot}$ white dwarf and the blue track has a cool donor star and the red track a hot donor star. We show the mass transfer rate derived using a white dwarf plus accretion disc model, GDR2 parallax data and multi-wavelength photometric measurements.

kept fixed and repeat this 50 times. From these solutions we determine the mean value and standard uncertainty. Although this is a fairly simple approach the mass transfer rate it is robust enough to make general conclusions from the results as a whole. In Table 5 we show the derived mass transfer rates. In Fig. 4 we show the mass transfer rate as a function of orbital period along with two predicted tracks from Bildsten et al. (2006) and we show the fit to the SED's in Fig. B.1.

In Fig. 4 we can see that some systems appear to lie close to the predicted evolutionary track of a M_1=0.65 $M_{\odot}$ and hot donor star. However, there is a tendency for sources to lie above this track. In two cases, SDSS J1908 and ASASSN-14mv, their mass transfer rate is several orders of magnitude greater than the hot donor track. SDSS J1908 lies above the predicted absolute magnitude for its orbital period by ~1 mag (Fig. 3), which is consistent with a higher mass transfer rate. On the other hand, ASASSN-14mv has an absolute magnitude consistent with expectations, which seems to be at odds with the high mass transfer rate. For the eclipsing system Gaia14aae, we predict a mass transfer rate of $\log 10 = -10.48$, which is within 3σ of the prediction ($\log 10 = -10.74$) based on using the absolute magnitude of the bright spot (Sect. 7.2). Despite these caveats, our results show evidence that the mass transfer rate for the majority of systems is higher than predicted from the models – and in some cases perhaps by an order of magnitude or more.

The most obvious reason for this result is that the donor star is larger – with a correspondingly higher mass transfer rate – than predicted. Indeed, recent observational work has shown that the donor star is larger than expected from white dwarfs models and in some cases larger than helium star models (Green et al. 2018a). Moreover, a detailed study of the eclipsing system Gaia14aae (Green et al. 2018c) were able to determine system parameters (M_1, M_2, R_1, R_2) to high accuracy. This suggests that this system is likely to have originated via the hydrogen CV evolutionary track. However, no hydrogen is observed in its spectrum as would be expected. These results taken with our findings should provide an impetus to revisiting the formation models.

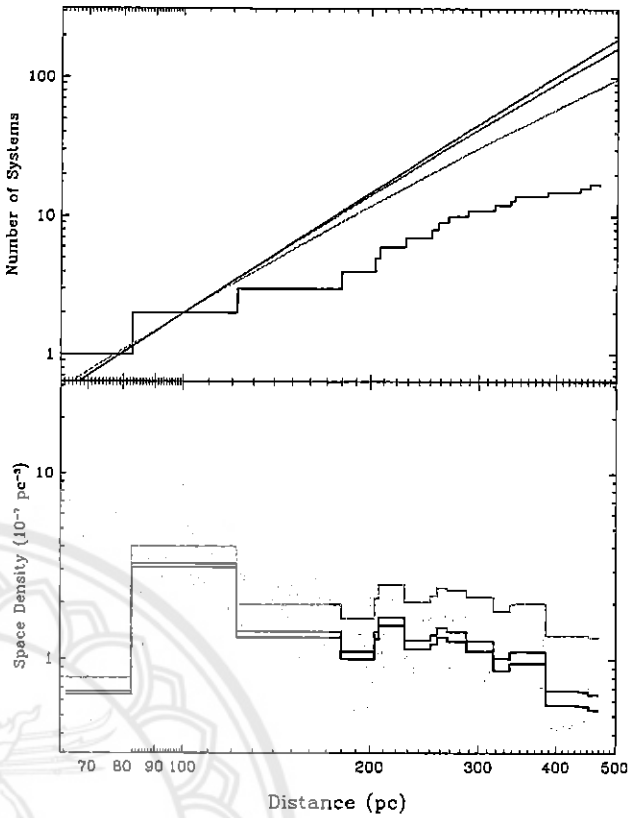

Fig. 5. *Top panel:* observed and predicted cumulative distribution of AM CVn stars as a function of distance. Predicted distributions are shown for Galactic disc models with three different exponential vertical scale heights: 100 pc (green), 300 pc (red) and 500 pc (blue). Given that AM CVn stars are thought to be preferentially old systems, the two larger scale heights are likely to be more appropriate for this population. All models have been normalised to the data at 100 pc. The clear discrepancy between models and data – which increases with distance – points to serious incompleteness in the observational sample. *Bottom panel:* space density (and 1σ error bands) as a function of distance, as estimated from the number of AM CVn stars and the effective volume contained within this distance. Effective volumes have been calculated for the same three Galactic disc models as shown in the top panel, thus providing three different space density estimates.

9. Space density of AM CVn stars

The AM CVn stars are at the very shortest period end of the binary star orbital period distribution and their space density is a sensitive test for binary evolutionary models. Together with the non-interacting double white dwarf binary, their number largely sets the astrophysical background for gravitational wave detectors such as LISA. Nelemans et al. (2001a) found that the space density of AM CVn stars was very uncertain and subject to uncertainties due to selection effects but determined a range of 0.4–1.7×10^{-4} pc^{-3} (limits being termed "pessimistic" and "optimistic" respectively).

With the advent of the large scale Sloan Digital Sky Survey (SDSS) it was possible to obtain optical spectra of stars which had colours consistent with the known AM CVn stars and therefore identify new systems in a systematic manner. Based on SDSS data (Roelofs et al. 2007a) found a space density of $1 - 3 \times 10^{-6}$ pc^{-3} – more than an order of magnitude lower than the pessimistic model of Nelemans et al. (2001b). Using a significantly expanded SDSS sample, Carter et al. (2013a) derived

Table 6. Results of searching for physically nearby stars to AM CVn stars..

	Gaia SourceID	RA J2000	Dec J2000	p (mas)	pmra (mas yr^{-1})	pmdec (mas yr^{-1})	G (mag)	$g-r$	Separation (pc)
KL Dra	2239471475135041664	291.159333	59.696233	1.04(15)	−2.46(30)	−18.27(26)	19.05	1.21	
	2239448930851818112	290.953649	59.610338	1.11(33)	−2.89(75)	−18.37(80)	19.44	1.14	3.5 ± 0.6
SDSS J1525+3600	1375131155313563136	231.289887	36.015117	1.93(28)	4.79(81)	−16.87(81)	19.665	0.60	
	1375135415921155968	231.150531	36.107433	1.63(60)	5.25(129)	−16.410(129)	20.226	1.13	1.4 ± 0.3
	1375131155313567232	231.288185	36.023225	2.28(15)	5.24(28)	−14.492(28)	18.293	1.20	0.06 ± 0.01

Notes. The candidate companion stars were selected by searching for stars within 3σ of the parallax to the AM CVn star and also 3σ of the proper motions in RA and Dec. In the final column we give the physical separation between the star and the AM CVn star.

an observed space density of $5 \pm 3 \times 10^{-7}$ pc^{-3}, a value which is even lower than that of Roelofs et al. (2007a), and is currently the most reliable estimate.

Perhaps the greatest source of uncertainty in predicting the space density lies in the relative importance of the formation channels. As we summarise in Sect. 1, there are three predicted channels – detached double white dwarfs that start mass transfer at very short orbital periods; systems in which a non-degenerate core helium burning star starts mass transfer and binaries in which a white dwarf is accreting from a semi-degenerate star (the hydrogen CV channel). The very low observed space density is compatible with only the double white dwarf contribution to the formation. So either there are many fewer systems coming from the helium star channel (and the CV channel) or we do not sufficiently understand which detached binaries turn into stable mass-transfer systems.

The main challenge in obtaining a space density estimate from the full sample of known AM CVn stars shown in Table 1 is that it contains systems discovered by a variety of different methods and surveys. For example, variability, the presence of emission lines and unusual colours have all been used to detect AM CVn stars. As a result, the sample in Table 1 is neither flux- nor volume-limited, but is instead affected by complex and often poorly understood selection effects. Determining completeness corrections for the entire sample with confidence is therefore impossible.

Nevertheless, the *Gaia* DR2 distances for the known AM CVn stars do contain crucial information. First, we can test if the sample is complete out to some limiting distance. If so, then a space density estimate can be derived immediately from this volume-limited subsample. Second, even if completeness cannot be established out to any distance, the sample can at least be used to set a firm lower limit on the space density.

Figure 5 shows the results of implementing these ideas. The top panel shows the cumulative distribution of AM CVn stars as a function of distance, compared to the expected distributions for stellar populations associated with the Galactic disc. It is immediately obvious that completeness cannot be established with confidence out to any distance. Based on this data set alone, it is quite possible that there is a significant population of undiscovered AM CVn stars, with systems waiting to be discovered even within $\simeq 100$ pc.

The bottom panel of Fig. 5 shows the space density one would estimate from the number of AM CVn stars as a function of distance, d. This is given by $N/V_{\rm eff}(d)$, where N is the number of systems found at distances smaller than d and $V_{\rm eff}$ is the effective volume contained within d in a given Galactic model. Since our sample is likely to be incomplete everywhere, these estimates must be treated as lower limits. The lower limit suggested by our highest space density estimate would be $\rho_0 > 3 \times 10^{-7}$ pc^{-3}. However, allowing for the Poisson errors affecting our small sample, our best 2σ limit is substantially weaker, $\rho_0 > 7 \times 10^{-8}$ pc^{-3}.

10. Searching for companion stars to the AM CVn stars

We performed a search to identify companions to those AM CVn stars which have a *Gaia* DR2 parallax determined to better than 20 percent. For each AM CVn star, we obtained the *Gaia* DR2 data for all sources within 20′, and then searched for stars which had a parallax and proper motion in RA and DEC within 3σ. Two AM CVn stars, KL Dra and SDSS J1525+3600, had nearby stars which fulfilled these criteria: their positions and properties are shown in Table 6.

We determined the physical separation between the candidate companion stars and show these in the final column of Table 6. The candidate companion star to KL Dra is 12.4′ distant (=3.5 pc), whilst for SDSSJ1525+3600 they are 8.4′ and 6.1″ (=1.4 pc and 0.06 pc or 1.25×10^5 AU). The more distant candidate companions are too distant to have any effect on the dynamics of the AM CVn binary, although they may have been much closer in the distant past. However, the candidate companion to SDSSJ1525+3600 is only 6.1″ distant providing powerful impetus to obtain a radial velocity measurement to determine whether it is physically associated with the AM CVn binary. If they do show similar velocities then they will be interesting from a binary formation and evolutionary point of view.

11. Conclusions

For the first time we have reliable distances to more than a few AM CVn stars. Using these distances we determine the expected cumulative distribution of AM CVn stars and compare it with the distribution of a Galactic disc population. We find that there is likely to be a significant number of AM CVn stars awaiting to be discovered. Since we find that the location of AM CVn stars are in a distinctive region of the HR diagram (Fig. 2) the *Gaia* DR2 dataset will be a useful tool for identifying candidate systems based on their colour and absolute magnitude.

One of the great uncertainties in predicting the space density of AM CVn stars has been in determining the relative importance of the three formation channels. There is now mounting evidence that the majority donor stars in AM CVn stars are not fully degenerate. We were able to determine the mass transfer rate in 15 AM CVn stars and find that most have rates which are

greater than predicted by standard tracks. The donors appear to be larger than expected.

We also find that none of the AM CVn stars which have proper motion and parallax data are likely to be halo objects. Those objects which have very low heavy element abundances are therefore not likely to be due to their age. Coupled with the findings that the parameters of the eclipsing AM CVn star, Gaia14aae, does not readily fit with the models should serve as impetus to revisit these models and the nature of the donor star in particular.

Acknowledgements. This work has made use of data from the European Space Agency (ESA) mission *Gaia* (https://www.cosmos.esa.int/gaia), processed by the *Gaia* Data Processing and Analysis Consortium (DPAC, https://www.cosmos.esa.int/web/gaia/dpac/consortium). Funding for the DPAC has been provided by national institutions, in particular the institutions participating in the *Gaia* Multilateral Agreement. We extracted GALEX data from Multi-Mission archive at the Space Telescope Science Institute (MAST). The Pan-STARRS1 Surveys (PS1) and the PS1 public science archive have been made possible through contributions by the Institute for Astronomy, the University of Hawaii, the Pan-STARRS Project Office, the Max-Planck Society and its participating institutes, the Max Planck Institute for Astronomy, Heidelberg and the Max Planck Institute for Extraterrestrial Physics, Garching, The Johns Hopkins University, Durham University, the University of Edinburgh, the Queen's University Belfast, the Harvard-Smithsonian Centre for Astrophysics, the Las Cumbres Observatory Global Telescope Network Incorporated, the National Central University of Taiwan, the Space Telescope Science Institute, the National Aeronautics and Space Administration under Grant No. NNX08AR22G issued through the Planetary Science Division of the NASA Science Mission Directorate, the National Science Foundation Grant No. AST-1238877, the University of Maryland, Eotvos Lorand University (ELTE), the Los Alamos National Laboratory, and the Gordon and Betty Moore Foundation. The national facility capability for SkyMapper has been funded through ARC LIEF grant LE130100104 from the Australian Research Council, awarded to the University of Sydney, the Australian National University, Swinburne University of Technology, the University of Queensland, the University of Western Australia, the University of Melbourne, Curtin University of Technology, Monash University and the Australian Astronomical Observatory. SkyMapper is owned and operated by The Australian National University's Research School of Astronomy and Astrophysics. The survey data were processed and provided by the SkyMapper Team at ANU. The SkyMapper node of the All-Sky Virtual Observatory (ASVO) is hosted at the National Computational Infrastructure (NCI). Development and support the SkyMapper node of the ASVO has been funded in part by Astronomy Australia Limited (AAL) and the Australian Government through the Commonwealth's Education Investment Fund (EIF) and National Collaborative Research Infrastructure Strategy (NCRIS), particularly the National eResearch Collaboration Tools and Resources (NeCTAR) and the Australian National Data Service Projects (ANDS). This research made use of Astropy, a community-developed core Python package for Astronomy (Astropy Collaboration 2018). Armagh Observatory and Planetarium is core funded by the Northern Ireland Executive through the Dept for Communities. MJG acknowledges funding from an STFC studentship via grant number ST/N504506/1. A.A. acknowledges the support of the National Research Council of Thailand (grant number R2561B087).

References

Abazajian, K. N., Adelman-McCarthy, J. K., Agüeros, M. A., et al. 2009, ApJS, 182, 543
Abbott, T. M. C., Robinson, E. L., Hill, G. J., & Haswell, C. A. 1992, ApJ, 399, 680
Anderson, S. F., Haggard, D., Homer, L., et al. 2005, AJ, 130, 2230
Anderson, S. F., Haggard, D., Homer, L., et al. 2008, AJ, 135, 2108
Astraatmadja, T. L., & Bailer-Jones, C. A. L. 2016, ApJ, 833
Astropy Collaboration (Price-Whelan, A. M., et al.) 2018, AJ, 156, 123
Bailer-Jones, C. A. L. 2015, PASP, 127, 119
Barros, S. C. C., Marsh, T. R., Dhillon, V. S., et al. 2007, MNRAS, 374, 1334
Bergeron, P., Wesemael, F., Dufour, P., et al. 2011, ApJ, 737, 28
Bessell, M., Bloxham, G., Schmidt, B., et al. 2011, PASP, 123, 789
Bianchi, L. 2014, Ap&SS, 354, 103
Bildsten, L., Townsley, D. M., Deloye, C. J., & Nelemans, G. 2006, ApJ, 640, 446
Breedt, E. 2015, Proc. Sci., 255, 25
Breedt, E., Gänsicke, B. T., Marsh, T. R., et al. 2012, MNRAS, 425, 2548
Breedt, E., Gänsicke, B. T., Drake, A. J., et al. 2014, MNRAS, 443, 3174
Campbell, H. C., Marsh, T. R., Fraser, M., et al. 2015, MNRAS, 452, 1060
Cannizzo, J. K., & Nelemans, G. 2015, ApJ, 803, 19
Cardelli, J. C., Clayton, G. C., & Mathis, J. S. 1989, ApJ, 345, 245
Carter, P. J., Marsh, T. R., Steeghs, D., et al. 2013a, MNRAS, 429, 2143
Carter, P. J., Steeghs, D., de Miguel, E., et al. 2013b, MNRAS, 431, 372
Carter, P. J., Steeghs, D., Marsh, T. R., et al. 2014a, MNRAS, 437, 2894
Carter, P. J., Gänsicke, B. T., Steeghs, D., et al. 2014b, MNRAS, 439, 2848
Cartier, R., Gutierrez, C. P., Smith, M., et al. 2017, ATel, 10334
Chambers, K. C., Magnier, E. A., Metcalfe, N., et al. 2016, ArXiv e-prints [arXiv:1612.05560]
Copperwheat, C. M., Marsh, T. R., Littlefair, S. P., et al. 2011, MNRAS, 410, 1113
Deloye, C. J., Bildsten, L., & Nelemans, G. 2005, ApJ, 624, 934
Deloye, C. J., Taam, R. E., Winisdoerffer, C., & Chabrier, G. 2007, MNRAS, 381, 525
Espaillat, C., Patterson, J., Warner, B., & Woudt, P. 2005, PASP, 117, 189
Fontaine, G., Brassard, P., Green, E. M., et al. 2011, ApJ, 726, 92
Gaia Collaboration (Brown, A. G. A., et al.) 2016a, A&A, 595, A2
Gaia Collaboration (Prusti, T., et al.) 2016b, A&A, 595, A1
Gaia Collaboration (Brown, A. G. A., et al.) 2018a, A&A, 616, A1
Gaia Collaboration (Lindegren, L., et al.) 2018b, A&A, 616, A2
Gaia Collaboration (Luri, X., et al.) 2018c, A&A, 616, A9
Gehron, K., Nagel, T., Rauch, T., & Werner, K. 2014, A&A, 562, A132
Green, G. M., Schlafly, E. F., Finkbeiner, D., et al. 2018a, MNRAS, 478, 651
Green, M. J., Marsh, T. R., Steeghs, D. T. H., et al. 2018b, MNRAS, 476, 1663
Green, M. J., Hermes, J. J., Marsh, T. R., et al. 2018c, MNRAS, 477, 5646
Holberg, J. B., & Bergeron, P. 2006, AJ, 132, 1221
Hollands, M. A., Tremblay, P.-E., Gänsicke, B. T., Gentile-Fusillo, N. P., & Toonen, S. 2018, MNRAS, 480, 3942
Iben, I. J., & Tutukov, A. V. 1987, ApJ, 313, 727
Kato, T., Stubbings, R., Monard, B., et al. 2004, PASJ, 56, S89
Kato, T., Ohshima, T., Denisenko, D., et al. 2014, PASJ, 66, L7
Kato, T., Hambsch, F.-J., & Monard, B. 2015, PASJ, 67, L2
Kepler, S. O., Pelisoli, I., Koester, D., et al. 2015, MNRAS, 446, 4078
Kong, X., Luo, A. L., Li, X. R., et al. 2018, PASP, 130, 084203
Korol, V., Rossi, E. M., Groot, P. J., et al. 2017, MNRAS, 470, 1894
Kotko, I., Lasota, J.-P., Dubus, G., & Hameury, J.-M. 2012, A&A, 544, A13
Kowalski, P. M., & Saumon, D. 2006, ApJ, 651, L137
Kupfer, T., Groot, P. J., Levitan, D., et al. 2013, MNRAS, 432, 2048
Kupfer, T., Groot, P. J., Bloemen, S., et al. 2015, MNRAS, 453, 483
Kupfer, T., Korol, V., Shah, S., et al. 2018, MNRAS, 480, 302
Levitan, D., Fulton, B. J., Groot, P. J., et al. 2011, ApJ, 739, 68
Levitan, D., Kupfer, T., Groot, P. J., et al. 2013, MNRAS, 430, 996
Levitan, D., Kupfer, T., Groot, P. J., et al. 2014, ApJ, 785, 114
Levitan, D., Groot, P. J., Prince, T. A., et al. 2015, MNRAS, 446, 391
Marsh, T. R. 1988, MNRAS, 231, 1117
Marsh, T. R., Horne, K., & Rosen, S. R. 1991, ApJ, 366, 535
Marsh, T. R., Nelemans, G., & Steeghs, D. 2004, MNRAS, 350, 113
Marsh, T., Parsons, S., & Dhillon, V. 2017, ATel, 10354
Martin, D. C., Fanson, J., Schiminovich, D., et al. 2005, ApJ, 619, L1
Motch, C., Haberl, F., Guillout, P., et al. 1996, A&A, 307, 459
Motsoaledi, M. 2015, Proc. Sci., 255, 16
Nagel, T., Rauch, T., & Werner, K. 2009, A&A, 499, 773
Nather, R. E., Robinson, E. L., & Stover, R. J. 1981, ApJ, 244, 269
Nelemans, G., Portegies Zwart, S. F., Verbunt, F., & Yungelson, L. R. 2001a, A&A, 368, 939
Nelemans, G., Steeghs, D., & Groot, P. J. 2001b, MNRAS, 326, 621
Nelemans, G., Yungelson, L. R., & Portegies Zwart, S. F. 2004, MNRAS, 349, 181
Nelemans, G., Yungelson, L. R., van der Sluys, M. V., & Tout, C. A. 2010, MNRAS, 401, 1347
Nissanke, S., Vallisneri, M., Nelemans, G., et al. 2012, ApJ, 758, 131
O'Donoghue, D., Kilkenny, D., Chen, A., et al. 1994, MNRAS, 271, 910
Osaki, Y. 1989, PASJ, 41, 1005O
Paczyński, B. 1967, Acta Astron., 17, 287
Pauli, E.-M., Napiwotzki, R., Altmann, M., et al. 2003, A&A, 400, 877
Pauli, E.-M., Napiwotzki, R., Heber, U., Altmann, M., & Odenkirchen, M. 2006, A&A, 447, 173
Piersanti, L., Yungelson, L. R., & Tornambé, A. 2015, MNRAS, 452, 2897
Prieto, J. L., Morrell, N., Grupe, D., et al. 2014, ATel, 6475
Ramsay, G., Hakala, P., & Cropper, M. 2002a, MNRAS, 332, L7
Ramsay, G., Wu, K., Cropper, M., et al. 2002b, MNRAS, 333, 575
Ramsay, G., Hakala, P., Marsh, T., et al. 2005, A&A, 440, 675
Ramsay, G., Groot, P. J., Marsh, T., et al. 2006, A&A, 457, 623
Ramsay, G., Barclay, T., Steeghs, D., et al. 2012, MNRAS, 419, 2836

Ramsay, G., Schreiber, M., Gänsicke, B. T., & Wheatley, P. J. 2017, A&A, 604A, 107
Rau, A., Roelofs, G. H. A., Groot, P. J., et al. 2010, ApJ, 708, 456
Roelofs, G. H. A. 2007, PhD Thesis, University of Nijmegen, The Netherlands
Roelofs, G. H. A., Groot, P. J., Marsh, T. R., et al. 2005, MNRAS, 361, 487
Roelofs, G. H. A., Nelemans, G., & Groot, P. J. 2007a, MNRAS, 382, 685
Roelofs, G. H. A., Groot, P. J., Benedict, G. F., et al. 2007b, ApJ, 666, 1174
Roelofs, G. H. A., Groot, P. J., Steeghs, D., et al. 2009, MNRAS, 394, 367
Ruiz, M. T., Rojo, P. M., Garay, G., & Maza, J. 2001, ApJ, 552, 679
Savonije, G. J., de Kool, M., & van den Heuvel, E. P. J. 1986, A&A, 155, 51
Scalzo, R. A., Yuan, F., Childress, M. J., et al. 2017, PASA, 34, 30
Schlafly, E. F., & Finkbeiner, D. P. 2011, ApJ, 737, 103
Shears, J., Brady, S., Koff, R., Goff, W., & Boyd, D. 2012, J. Br. Astron. Assoc., 122, 49
Shen, K. J. 2015, ApJ, 805, L6
Solheim, J.-E. 2010, PASP, 122, 1133
Thorstensen, J. R., & Skinner, J. N. 2012, AJ, 144, 81
Tonry, J. L., Stubbs, C. W., Lykke, K. R., et al. 2012, ApJ, 750, 99
Tremblay, P.-E., Bergeron, P., & Gianninas, A. 2011, ApJ, 730, 128
Verbunt, F., & Rappaport, S. 1988, ApJ, 332, 193
Wagner, R. M., Kaur, A., Porter, A., et al. 2014, ATel, 6669
Wevers, T., Torres, M. A. P., Jonker, P. G., et al. 2016, MNRAS, 462, L106
Wood, M. A., Winget, D. E., Nather, R. E., et al. 1987, ApJ, 313, 757
Wood, M. A., Casey, M. J., Garnavich, P. M., & Haag, B. 2002, MNRAS, 334, 87
Wood, M. A., Still, M. D., Howell, S. B., et al. 2011, ApJ, 741, 105
Wood-Vasey, W. M., Aldering, G., Nugent, P., & Li, K. 2003, IAUC, 8077
Woudt, P. A., Warner, B., & Rykoff, E. 2005, IAUC, 8531
Woudt, P. A., Warner, B., & Motsoaledi, M. 2013, ATel, 4726
York, D. G. 2000, AJ, 120, 1579

Appendix A: Photometry of AM CVn stars: online table

We provide an online table in fits format[1] which includes data on all of the known AM CVn stars. The columns and caveats are described below.

A.1. Target names and coordinates

In the main body of the paper (e.g. Table 1), we use IAU Variable Star names or shortened survey IDs for each of the targets. The online table includes these IDs (Col. 1), as well as alternative names by which each target is known (Col. 2).

We give the J2015.5 coordinates from *Gaia* where available (Cols. 5, 6), as well as ICRS J2000.0 coordinates for all sources (Cols. 3, 4). The J2000.0 coordinates were derived from the *Gaia* 5-parameter astrometry where available, otherwise the table shows the most precise coordinates available for that target. We also computed the IAU 1958 Galactic latitude and longitude for each target. These are given in Cols. 7 and 8.

The *Gaia* DR2 source ID is shown in Col. 9.

A.2. Orbital period and brightness range

Columns 10 and 11 show the period of the binary in days and minutes respectively, with a flag/comment in Col. 12 to indicate whether the period is the orbital period ("orb", most reliably measured from time series spectroscopy), the superhump period ("sh", resulting from disc precession during the outburst and typically a few per cent longer than the orbital period), estimated from the outburst recurrence time ("est rec", Levitan et al. 2015) or whether no period has been measured for the system so far ("unknown"). References for the discovery and the period measurements are indexed in Col. 15, corresponding to the following references:

[1] Ramsay et al. 2002a, [2] Ramsay et al. 2002b, [3] Espaillat et al. 2005, [4] Nelemans et al. 2001b, [5] Fontaine 2011, [6] Kupfer et al. 2015, [7] O'Donoghue et al. 1994, [8] Levitan et al. 2014, [9] Wevers et al. 2016, [10] Kato et al. 2015, [11] Wood et al. 1987, [12] Wood et al. 2002, [13] Kato et al. 2004, [14] Levitan et al. 2015, [15] Levitan et al. 2011, [16] ASASSN `http://www.astronomy.ohio-state.edu/~assassin/transients.html`, [17] AAVSO `https://www.aavso.org`, [18] Copperwheat et al. 2011, [19] Abbott et al. 1992, [20] Levitan et al. 2013, [21] Thorstensen & Skinner 2012, [22] Motsoaledi 2015, [23] Wood-Vasey et al. 2003, [24a] Carter et al. 2014a, [24b] Carter et al. 2014b, [25] Woudt et al. 2005, [26] Shears et al. 2012, [27] Roelofs et al. 2005, [28] Roelofs et al. 2009, [29] Anderson et al. 2005, [30] Ramsay et al. 2012, [31] Rau et al. 2010, [32] Nather et al. 1981, [33] Prieto et al. 2014, [34] Woudt et al. 2013, [35] Kato et al. 2014, [36] Campbell et al. 2015, [37] Marsh et al. 2017, [38] Anderson et al. 2008, [39] Kupfer et al. 2013, [40] Kepler et al. 2015, [41] Wagner et al. 2014, [42] Ruiz et al. 2001, [43] Green et al. 2018c, [44] Kato, vsnet-alert 18124, [45] Aungwerojwit et al. (in prep.), [46] Breedt et al. (in prep.), [47] Kupfer et al. (in prep.), [48] Maehara & Kojima, vsnet-alert 22174, [49] Green et al. 2018b, [50] Kong et al. 2018.

The Y/N flag in Col. 13 indicates whether the system has been observed in outburst, and the magnitude range (with filter information) is given in Col. 14.

A.3. Parallax, reddening and derived quantities

The calculation of the following quantities were discussed in detail in the main text:

Columns 16–17: parallax and error (mas), taken from *Gaia* DR2.

Columns 18–19: distance and error (pc) — calculated from an exponentially decreasing space density prior with $L = 400$ pc. See Sect. 3.

Columns 20–21: extinction and reddening parameters $E(B-V)$ and A_g towards each system (mag), derived from the Pan-STARRS1 distance reddening maps (Green et al. 2018a) as discussed in Sect. 5. ASASSN-14cc, ASASSN-14ei, NSV1440 and Gaia16all have parallax measurements from *Gaia*, but are not in the Pan-STARRS1 footprint. For these four stars we show the maximum reddening from Schlafly & Finkbeiner (2011). A note has been added in Col. 66 of the table.

Column 22: g band quiescent magnitude taken from Pan-STARRS, used to calculated the absolute magnitude.

Columns 23–24: absolute magnitude M_g and its associated error (mag).

A.4. GALEX

Although *Swift* and *XMM-Newton* has been used to observe some AM CVn stars, GALEX provided the opportunity to take an unbiased snapshot survey of their near UV flux. GALEX was launched in April 2003 and had a lifetime of ten years and performed observations at UV wavelengths (Martin 2005). It had a primary mirror 50 cm in diameter and had a field of view of 1.25°. It had two UV channels, the Near UV (NUV, central wavelength 2271Å) and the Far UV (FUV, 1528 Å), the latter failing after 6 years. Whilst it could perform relatively short pointed observations, it also carried out a wide field survey and by its end it had sampled 3/4 of the sky in one UV band (Bianchi 2014). 41 of the known AM CVn stars are included in the catalogue of Bianchi (2014). We show the FUV and NUV fluxes in units of mJy in Cols. 25–26 (FUV) and Cols. 27–28 (NUV) of the online table.

A.5. SDSS

The Sloan Digital Sky Survey (SDSS) uses a 2.5m telescope at Apache Point Observatory in New Mexico, and has a field of view three degrees across (York 2000). Its Data Release 7 includes a photometric catalogue of northern-hemisphere targets (Abazajian et al. 2009).

We performed a cross-match of known AM CVn J2000.0 positions with all SDSS photometric objects, using a search radius of 2 arcsec. We identified 34 AM CVns which have SDSS photometry. All but two of these magnitudes are consistent with the faint end of the range shown in Table 1. The two outliers are SDSS J0804+1616, which is brighter by approximately 0.7 mag (perhaps consistent with the large-scale variability this system shows even in quiescence; Roelofs et al. 2009) and PU Aqr=SDSS J2047+0008, which is brighter by approximately 1.8 mag and may have been in outburst or in decline from outburst when the SDSS data were collected.

The SDSS *ugriz* magnitudes and their errors are shown in columns 29–38 of the online table.

[1] Available at the CDS and at `https://www.ast.cam.ac.uk/~ebreedt/web/AMCVn_datatable_Ramsay_etal_2018.fits`

Table A.1. PanSTARRS1 measurements of these three AM CVn stars appears to have been taken in different accretion states in the different bands.

Source	g	r	i	z	y
CR Boo	16.630(42)	14.406(130)	14.965(92)	15.154(142)	15.494(96)
range	16.61..16.78	14.12..16.74	14.56..15.65	14.47..17.07	15.27..17.41
SDSS J0804+1616	18.222(61)	18.432(44)	18.556(26)	18.639(33)	18.493(29)
range	18.09..18.60	18.21..18.60	18.50..18.77	18.50..18.86	18.25..18.92
CRTS J0744+3254	21.345(275)	18.884(21)	21.397(55)	17.803(23)	18.298(16)
range	21.32..21.87	18.81..18.91	21.30..21.50	17.81..17.89	18.29..18.32

Notes. In addition to the magnitudes shown in the online table (and repeated here for clarity), we also show the range in magnitude for the detections in each filter.

A.6. Pan-STARRS1

Pan-STARRS1 is a 1.8m telescope with a field of view of seven square degrees, located on Halakala Observatory in Hawaii. There are five broad-band filters which are close to, but not exactly, the SDSS filters *grizy* (Chambers et al. 2016; Tonry 2012). It is performing an all-sky survey with declinations $> -30°$.

We performed a cross-match with Pan-STARRS1 DR1 using a 2 arcsec match radius to account for uncertainty in the recorded positions of the AM CVn stars. The mean AB PSF *grizy* magnitudes are shown in columns 39–48 of the online table for all systems which were found to have a match.

For those AM CVn stars which do not show outbursts the mean g mag is consistent with the values shown in Table 1. For those systems which do show outburst, Pan-STARRS1 has a mean magnitude which is consistent with the source being in quiescent apart from three systems: CR Boo where g is more consistent with it being in quiescent and the other filters in outburst; SDSS J0804+1616 has range in magnitude in Table 1 between 17.8–19.0 and the mean Pan-STARRS1 mag appears in the middle of this range and CRTS J0744+3254 which has a Pan-STARRS1 g mag much fainter than r. The Pan-STARRS1 DR1 gives a mean magnitude of the source over the pointings covered. However, it also gives a range in magnitudes for the different filters. For the three sources which show evidence for being in different accretion states, we show in Table A.1 the range in these filters' measurements.

A.7. Skymapper

Skymapper is a telescope with a 1.35m primary mirror located Siding Spring Observatory, Australia, and has a camera which covers 2.4×2.3 degrees of the sky (Scalzo 2017). Its primary goal is to obtain a map of the southern sky in a number of filters, with periods of poor conditions being focussed on detecting transients. There are six filters, with the bluest u, v, being narrow band filters ($FWHM = 42$ and 28 nm respectively) which cover the SDSS u band. The filters *griz* differ compared to their SDSS equivalents by 40 nm in effective wavelength and width (Bessell et al. 2011).

We performed a 2 arcsec radius cross-match with the Skymapper DR1.1 release and find that six AM CVn stars have at least one detection in one filter. We show the magnitudes in the *uvgrzi* filters on the AB mag scale in columns 49–60 of the online table.

A.8. Kinematics

Columns 61–64 list the proper motions in RA and Dec (mas) from *Gaia* DR2. The population membership (thick/thin disc of the Galaxy), as computed in Sect. 4, is shown in Col. 65. For convenience, these data are also shown in Table B.1.

The final column in the online table, 66, is a text field for specific notes about the data for that target.

Appendix B: SEDs and kinematic data

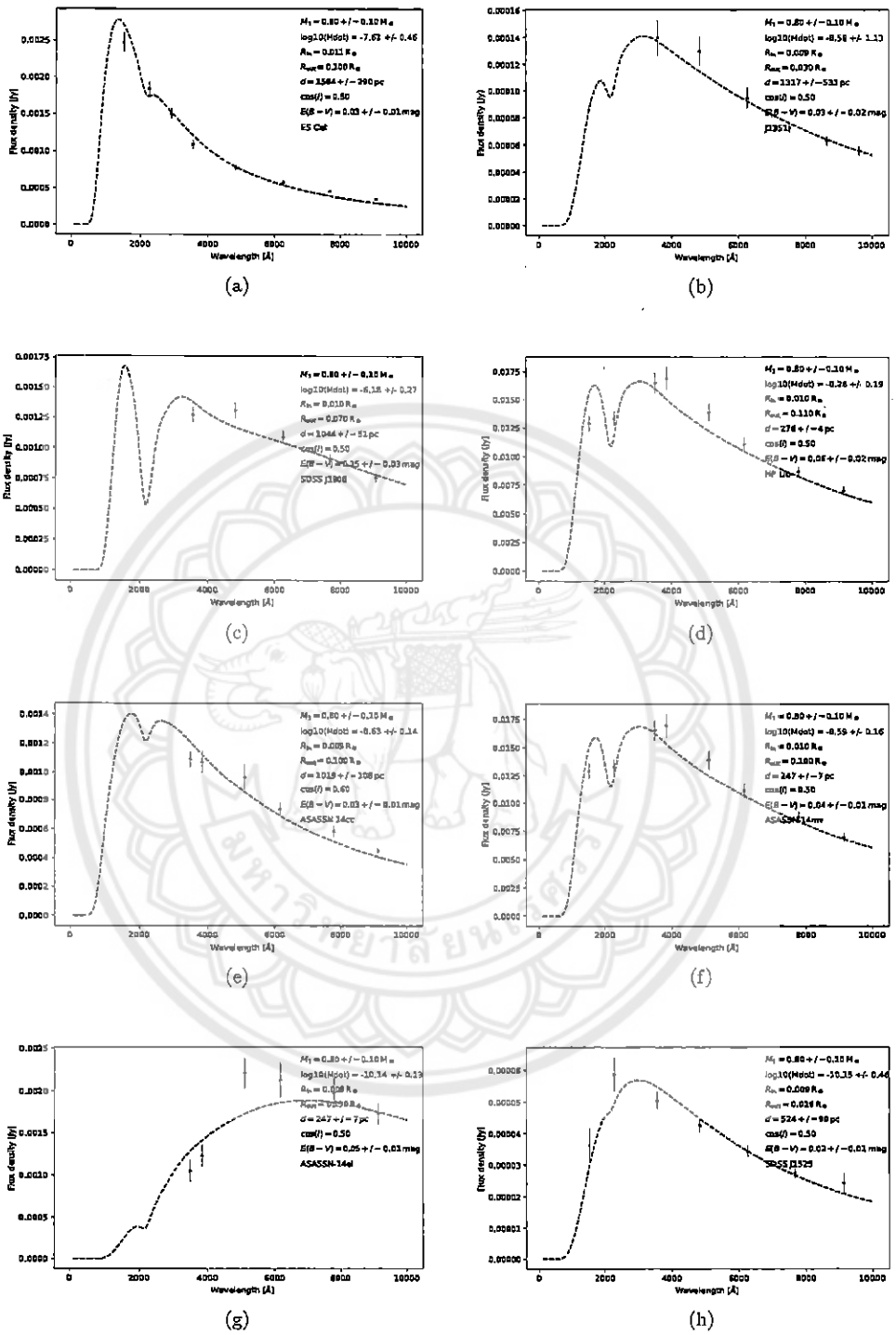

Fig. B.1. Spectral energy distribution of AM CVn stars which have a parallax accurate to within 20 percent and have multi-colour survey data in more than two filter passbands. In the solid line we show the model spectral energy distribution where M_1, E_{B-V} and distance are restricted to the values shown in each panel and the mass transfer rate, $\dot{M}$, is a free parameter.

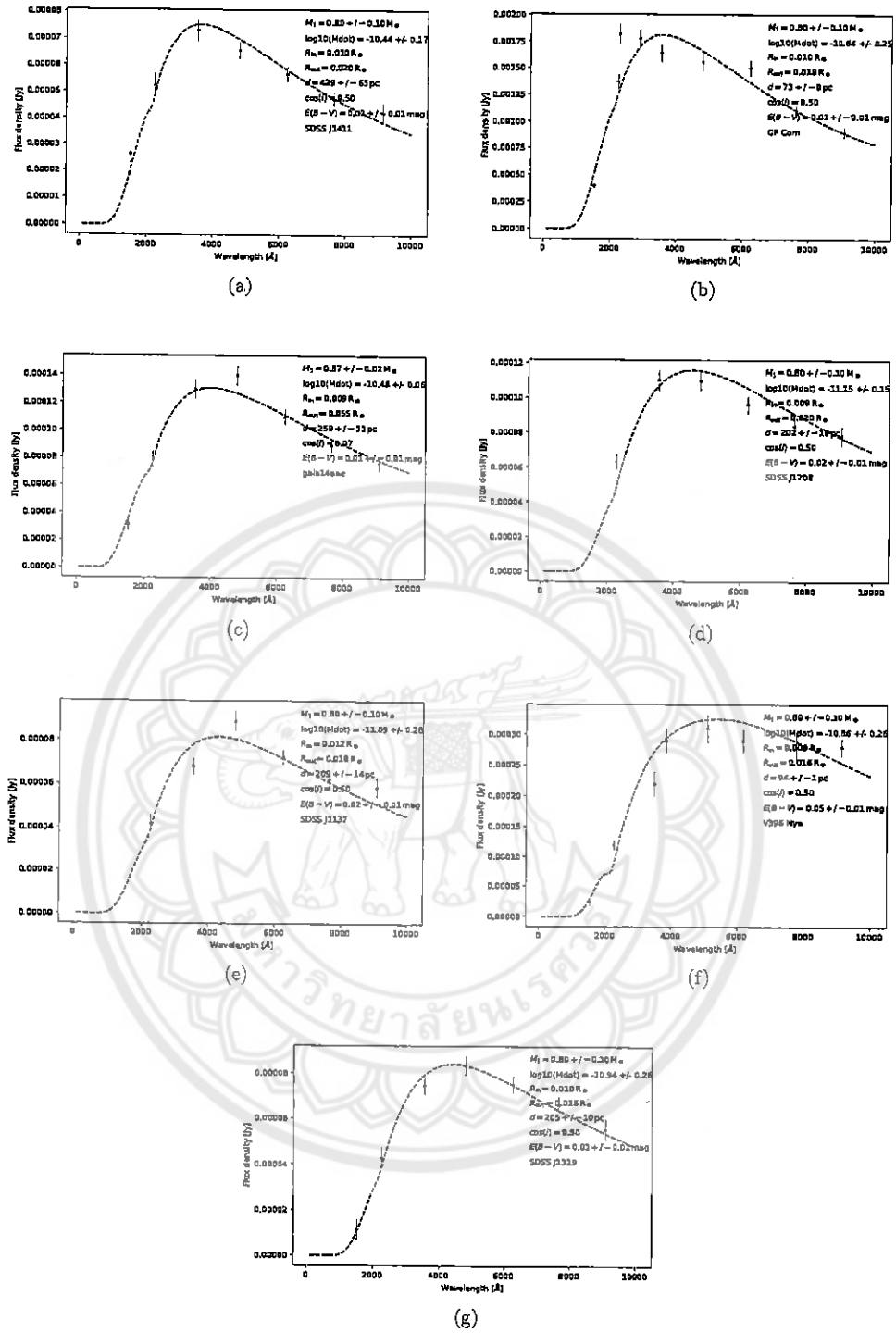

Fig. B.1. continued.

Table B.1. Kinematic information for the AM CVn stars with measured proper motions in *Gaia* DR2.

Source	pmra (mas yr^{-1})	pmdec (mas yr^{-1})	Population
V407 Vul	−2.315 ± 0.386	−3.726 ± 0.719	Thin
ES Cet	17.486 ± 0.196	−3.075 ± 0.157	Thick
SDSS J1351-0643	5.503 ± 0.586	−17.328 ± 0.465	Thick
AM CVn	30.935 ± 0.073	12.420 ± 0.053	Thick
SDSS J1908+3940	−7.019 ± 0.087	−5.332 ± 0.093	Thin
HP Lib	−28.776 ± 0.099	−12.636 ± 0.074	Thin
PTF1 J1919+4815	5.548 ± 0.535	5.850 ± 0.830	Thin/thick
CX361	2.393 ± 0.344	−2.001 ± 0.288	Thin
ASASSN-14cc	−14.897 ± 0.115	−37.800 ± 0.111	Thick
KL Dra	−2.463 ± 0.296	−18.269 ± 0.262	Thick
PTF1 J0719+4858	4.276 ± 0.297	2.345 ± 0.166	Thin
YZ LMi	−30.506 ± 0.841	−4.072 ± 1.084	Thin
CP Eri	18.090 ± 1.445	−7.174 ± 1.550	Thin
SDSS J1043+5632	−0.561 ± 0.936	−2.997 ± 1.099	Thin
CRTS J0910-2008	3.730 ± 1.050	−8.610 ± 0.923	Thin/thick
CRTS J0105+1903	7.159 ± 1.023	8.640 ± 0.923	Thin
V406 Hya	−1.429 ± 1.606	−6.191 ± 1.389	Thin
SDSS J1730+5545	4.104 ± 0.829	−33.861 ± 0.931	Thick
NSV1440	7.737 ± 0.255	27.446 ± 0.277	Thin
V558 Vir	−13.989 ± 2.482	−3.959 ± 3.140	Thin
SDSS J1240-0159	−1.852 ± 1.248	−8.006 ± 0.646	Thin
V744 And	−2.691 ± 0.827	6.332 ± 1.797	Thick
SDSS J1721+2733	2.815 ± 0.923	−2.025 ± 1.102	Thin
ASASSN-14mv	−17.270 ± 0.266	−43.836 ± 0.205	Thin
ASASSN-14ei	−10.263 ± 0.074	−15.380 ± 0.098	Thin
SDSS J1525+3600	4.787 ± 0.518	−16.876 ± 0.810	Thin
SDSS J0804+1616	1.365 ± 0.382	−5.972 ± 0.219	Thin
SDSS J1411+4812	−17.297 ± 0.431	36.323 ± 0.444	Thick
GP Com	−344.791 ± 0.131	34.743 ± 0.082	Thin/thick
SDSS J0902+3819	−15.799 ± 1.170	−13.360 ± 1.058	Thin
Gaia14aae	−3.927 ± 0.317	−14.099 ± 0.269	Thin
SDSS J1208+3550	−112.865 ± 0.651	−56.236 ± 0.510	Thick
SDSS J1642+1934	−2.560 ± 1.034	−28.606 ± 1.082	Thick
SDSS J1552+3201	5.943 ± 0.947	−27.253 ± 1.174	Thin
SDSS J1137+4054	23.118 ± 0.383	−56.566 ± 0.336	Thin
V396 Hya	−286.331 ± 0.306	−59.209 ± 0.213	Thick
SDSS J1319+5915	−27.885 ± 0.498	12.375 ± 0.359	Thin
CRTS J0844-0128	−5.291 ± 1.621	−4.794 ± 0.549	Thin
SDSS J1505+0659	44.487 ± 0.724	−25.417 ± 0.686	Thin/thick
Gaia 16all	−2.640 ± 1.647	5.287 ± 1.465	Thin

Notes. These data are also included in the online table.